



HAL
open science

Mid- to Late-Holocene Mediterranean climate variability: Contribution of multi-proxy and multi-sequence comparison using wavelet analysis in the north western Mediterranean basin.

Julien Azuara, Pierre Sabatier, V. Lebreton, Bassem Jalali, Marie-Alexandrine Sicre, Laurent Dezileau, Maria-Angela Bassetti, Jaime Frigola, Nathalie Combourieu-Nebout

► To cite this version:

Julien Azuara, Pierre Sabatier, V. Lebreton, Bassem Jalali, Marie-Alexandrine Sicre, et al.. Mid-to Late-Holocene Mediterranean climate variability: Contribution of multi-proxy and multi-sequence comparison using wavelet analysis in the north western Mediterranean basin.. *Earth-Science Reviews*, 2020, 208, pp.103232. 10.1016/j.earscirev.2020.103232 . hal-02569574

HAL Id: hal-02569574

<https://hal.science/hal-02569574v1>

Submitted on 25 Nov 2020

HAL is a multi-disciplinary open access archive for the deposit and dissemination of scientific research documents, whether they are published or not. The documents may come from teaching and research institutions in France or abroad, or from public or private research centers.

L'archive ouverte pluridisciplinaire **HAL**, est destinée au dépôt et à la diffusion de documents scientifiques de niveau recherche, publiés ou non, émanant des établissements d'enseignement et de recherche français ou étrangers, des laboratoires publics ou privés.



Distributed under a Creative Commons Attribution - NonCommercial - ShareAlike 4.0 International License

1 **Mid- to Late-Holocene Mediterranean climate variability: Contribution of**
2 **multi-proxy and multi-sequence comparison using wavelet spectral analysis**
3 **in the northwestern Mediterranean basin.**

4 Azuara Julien^{a*}, Sabatier Pierre^b, Lebreton Vincent^a, Jalali Bassem^c, Sicre Marie Alexandrine^d,
5 Dezileau Laurent^e, Bassetti Maria Angela^f, Frigola Jaime^g, Coumbourieu-Nebout Nathalie^a

6 ^aHNHP, Muséum National d'Histoire Naturelle, UMR CNRS 7194, 75013 Paris, France

7 ^bEDYTEM, Univ. Grenoble Alpes, Univ. Savoie Mont Blanc, UMR CNRS 5204, 73000 Chambéry,
8 France

9 ^cGEOGLOB, Université de Sfax, Faculté des Sciences de Sfax, 3038, Sfax, Tunisia

10 ^dLOCEAN, Sorbonne Universités (UPMC, Univ Paris 06), UMR CNRS-IRD-MNHN 7159, 75005
11 Paris, France.

12 ^eM2C, Université de Caen, UMR CNRS 6143, 14000 Caen, France

13 ^fCEFREM, Université de Perpignan, UMR CNRS 5110, 66000 Perpignan, France

14 ^gCRG Marine Geosciences, Department of Earth and Ocean Dynamics, Faculty of Earth Sciences,
15 Universitat de Barcelona, 08028 Barcelona, Spain

16 *Julien.azuara@mnhn.fr

17 **Keywords**

18 Holocene ; Paleoclimatology ; Climate dynamics ; Mediterranean ; Wavelet spectral analysis ;
19 Continental biomarkers ; Marine biomarkers ; Sediment mineralogy ; Vegetation dynamics

20 **Abstract**

21 Forcing and mechanisms underlying Holocene climate variability still remain poorly understood. This
22 work review already published paleoclimatic time series and proposes an alternative way to compare
23 them using spectral analysis. Such an approach may emphasize joint features between different signals
24 and lead us closer to the causes of past climate changes.

25 Seven paleoclimatic proxy records from 2 sequences from the Gulf of Lion were compiled. These
26 paleoclimate time-series were supplemented with proxies of the Atlantic area, the solar activity and a
27 sequence recording El Niño–Southern Oscillations (ENSO) past variability. A comparison of their
28 frequency content is proposed using wavelet spectral analysis for unevenly sampled time series. A new
29 algorithm is used in order to propagate the age model errors within wavelet power spectra.

30 Two main groups of shared spectral features specific to the Mid- and Late Holocene (after 8200 yrs cal
31 BP) can be defined on the basis of the results of these analyses, an Atlantic spectral feature (~1500 yrs)
32 and two possible tropical Pacific spectral features (600-700 and 2000-2200 yrs). The Atlantic cyclic
33 period is probably related to fluctuations of the Atlantic thermohaline circulation which would induce
34 changes in the storm track extension and position thereby impacting upon precipitation and storminess

35 over a millennial scale. The ENSO variability spectral features which are registered in the Gulf of Lion
36 proxies, potentially highlight a possible link between the tropical Pacific and the western Mediterranean
37 climates during the Mid to late Holocene that needs to be further investigated.

38 **Introduction**

39 Until recently, the Holocene was often referred to as a stable climatic period. However, with the
40 increasing resolution and diversity of paleoclimatic proxies, Holocene climate variability has
41 progressively come to light. Interest in Holocene climate variability really started in the late 90s, when
42 major features of this period became evident, such as the 8.2 kyrs event (Alley et al. 1997), Bond cycles
43 (Bond et al. 1997, 2001) or the abrupt end of the African Humid Period (deMenocal et al. 2000). The
44 development of this research field has followed increasing interest in current anthropogenic climate
45 change. Indeed, disentangling changes induced by increased greenhouse gases in the atmosphere from
46 the natural centennial scale climate variability is a crucial issue (Stocker et al. 2013).

47 Holocene rapid climate changes (RCCs) are now reported in many areas all over the world and by
48 numerous types of proxies (Mayewski et al. 2004). Nevertheless, RCCs are not yet fully understood and
49 the comparison of paleoclimatic proxies by simply comparing their curves can be confusing and
50 frustrating when the number of time series increases. In this case, an alternative approach is to compare
51 the time series in the frequency domain using spectral analysis in order to better understand the processes
52 which generate their variability and possibly uncover underlying connections between them. However,
53 spectral analyses classically apply to evenly sampled times series whereas paleoclimatic time series have
54 an irregular temporal sampling. To overcome this issue, specific tools for spectral analysis of
55 paleoclimatic time series have been developed in the past decades. Methods based on the Lomb-Scargle
56 Fourier transform (Lomb 1976, Scargle 1982) for unevenly spaced data in combination with the Welch-
57 Overlapped-Segment-Averaging algorithm (Welch 1967) were developed to deal specifically with
58 paleoclimatic time-series avoiding the distortions associated with resampling at regular time steps
59 (Schulz and Stattegger 1997, Schulz and Mudelsee 2002, Lenoir and Crucifix 2018a). Cross-spectral
60 analyses relying on the same approach have also been developed to compare quantitatively paleoclimatic
61 time series in the frequency domain (Björg Ólafsdóttir et al. 2016). Paleoclimatic time series are also
62 affected by uncertainties inherent to age-depth models and thus, algorithms have been developed to
63 account for timescale errors due to age-depths models in such analyses, showing the influence of those
64 errors on both spectral peak uncertainties and significance (Mudelsee et al. 2009, Rhines and Huybers
65 2011). Finally, the non-stationarity of the climate variability can be investigated by adapting wavelet
66 spectral analysis to irregularly sampled time series allowing time/frequency analysis of paleoclimatic
67 time series (Foster 1996, Lenoir and Crucifix 2018b, Polanco-Martinez and Faria 2018, Ghaderpour et
68 al. 2018, Ghaderpour et al. 2019). Indeed, unlike the previous methods based on the Lomb-Scargle
69 Fourier transform, wavelet spectral analysis can be applied to non-stationary time series whose periodic
70 features are not observed over their entire time range. Their application to paleoclimatic time series has

71 highlighted the importance of non-stationarities to understand past climate variability (e.g. Witt and
72 Schumann 2005, Polanco-Martinez and Faria 2018)

73 RCCs are detected by means of numerous proxies all over the Mediterranean basin: vegetation changes
74 (e.g. Jalut et al. 2009, Combourieu-Nebout et al. 2009, Fletcher et al. 2013, Sadori et al. 2015, Jimenez-
75 Moreno et al. 2015, Jaouadi et al. 2016), Sea Surface Temperature (SST) estimates (e.g. Sicre et al.
76 2016, Jalali et al. 2017), high molecular weight n-alkanes (e.g. Jalali et al. 2017), stable isotope analysis
77 on speleothems (e.g. Bar-Matthews and Ayalon 2011, Smith et al. 2016), lake level fluctuations (e.g.
78 Magny et al. 2002, 2003, 2007), flood frequencies (e.g. Wirth et al. 2013, Sabatier et al. 2017),
79 thermohaline circulation proxies (e.g. Frigola et al. 2007, Siani et al. 2013), changes in windiness (e.g.
80 Costas et al. 2016) or even storminess (e.g. Zazo et al. 2008, Billeaud et al. 2009, Sorrel et al. 2009,
81 Dezileau et al. 2011, 2016, Sabatier et al. 2012, Raji et al. 2015, Degeai et al. 2015, Orme et al. 2016),
82 glacier advances (e.g. Giraudi 2005, Giraudi et al. 2011), African dust inputs (Bout-Roumazeille et al.,
83 2013; Sabatier et al., 2020), etc. Nevertheless, while all of these proxies exhibit centennial scale climate
84 variability, the timing of the RCC intervals often differs from one sequence to another. Taken together,
85 these proxies reveal a very complex picture of Holocene climate variability within the Mediterranean
86 Basin. Some authors stress the existence of contrasting geographical patterns, which structure climate
87 variability and which can partly explain these discrepancies (Roberts et al. 2011, Magny et al. 2012,
88 2013, Peyron et al. 2013, Jalali et al. 2017). However, even within a restricted area, the correlation
89 between RCCs is not always straightforward and age model uncertainties cannot account for all of the
90 observed differences.

91 In order to better understand such complex patterns of climate variability in the Mediterranean region,
92 we further develop a wavelet spectral analysis approach used by Witt and Schumann (2005) to deal with
93 the non-stationarity of climate variability, and apply it to a set of climate proxies from a restricted area,
94 the Gulf of Lion, to discuss past climate changes over a restricted time period, the Mid- and Late-
95 Holocene from 8200 yrs cal BP to the present (Walker et al. 2012). We use an improved wavelet spectral
96 analysis algorithm for irregularly sampled time series (Lenoir and Crucifix 2018b) and develop a new
97 method to propagate age models' errors within wavelet spectral analysis, with a view to improving the
98 reliability of wavelet spectra comparison. Additionally, the cross spectral analysis method proposed by
99 Björg Ólafsdóttir et al. (2016) is used as a complementary tool to quantitatively compare the spectral
100 content of the studied time series. The proxies used were produced within the framework of the
101 MISTRALS/PaleoMeX research project. They are supplemented by published sequences from the near
102 Atlantic area (northwestern Spain, inner Bay of Biscay) and time series recording possible drivers (solar
103 variability) or major modes of climate variability (ENSO). Based on this dataset, our study aims to i)
104 identify forcing influencing western Mediterranean climate variability over the past 8000 years, ii)
105 investigate possible links between climate variability in this specific key region and the Atlantic or
106 tropical areas, and iii) review elements of climatology that may explain the links we detect between the
107 studied paleoclimatic time series.

108 **Geographical and climatic context**

109 The Gulf of Lion is a crescent-shaped continental margin located in the northwestern Mediterranean
110 basin. It is surrounded by relatively narrow coastal plains and important mountain ranges within the
111 hinterland of the eastern Pyrenees, the Massif Central and the Southern Alps (Figure 1). The coastal
112 plains are bordered by numerous brackish lagoons that are the result of the interaction between a process
113 of shore line regularization through the migration of sandy barriers, resulting from sediment transfer
114 through littoral hydrodynamics, and the filling of these areas by fluvial and marine inputs (Raynal et al.
115 2009, Sabatier et al. 2010). The Massif Central and the Southern Alps are separated by the Rhône Valley.
116 The Rhône, one of the major Mediterranean rivers, flows into the Mediterranean Sea in the eastern part
117 of the Gulf of Lion, forming a wide delta and supplying large amounts of sediment (31 Mt yr⁻¹; Ludwig
118 et al. 2009). Its wider drainage basin is influenced by both Mediterranean and temperate climates. The
119 continental margin has a maximum width of 72 km with a water depth ranging between approximately
120 0 and 100m. Further offshore, the shelf slopes abruptly to the 2000 m deep abyssal plain (Bassetti et al.
121 2016).

122 This region is under the influence of a Mediterranean climate with cool mild winters and dry hot
123 summers. In the lowlands, mean annual rainfall ranges from 500 to 800 mm (Rameau et al. 2008) with
124 a maximum in autumn when cumulated October precipitations reach around 80mm, and a minimum in
125 summer with cumulated July precipitations of less than 20mm (Météo France data, 1981-2010). Mean
126 annual temperature is between 12 and 16°C (Rameau et al. 2008) with a maximum of around 23°C in
127 July (monthly average) and a minimum of around 7°C in January (monthly average) (Météo France
128 data, 1981-2010). However, the steep altitudinal gradient results in a decrease of seasonality with
129 altitude. July precipitation increases with altitude while mean temperature decreases.

130 Large scale circulation patterns over the North Atlantic and Europe directly influence the western
131 Mediterranean (Plaut and Simmonet 2001). Persistent high-pressure systems over the Arctic regions
132 (Greenland, Iceland) and over Scandinavia tend to advect more Atlantic lows and rainfall toward the
133 western Mediterranean. In contrast, when the Atlantic subtropical anticyclone (Azores high) shifts
134 northwards, precipitation decreases. These large-scale circulation patterns also influence wind
135 circulation. An anticyclonic blocking over the eastern Atlantic, associated with a low-pressure system
136 over the central Mediterranean, induces cold, dry, northerly winds over the Gulf of Lion (Mistral and
137 Tramontane, Figure 1) (Najac et al. 2009; Sicre et al. 2016), while persistent high-pressure systems over
138 Scandinavia induce warm, humid, south-easterly winds (Plaut and Simonet 2001). Finally, large scale
139 circulation patterns can contribute to the triggering of extreme climate events such as Heavy
140 Precipitation Events (HPE; higher than 200mm in a day) (Joly et al. 2012, Nuissier et al. 2011) or
141 summer heat waves (Cassou et al. 2005). Latitudinal shifts of the Atlantic zonal storm track associated
142 with this general atmospheric circulation also influence the frequency and the intensity of northern

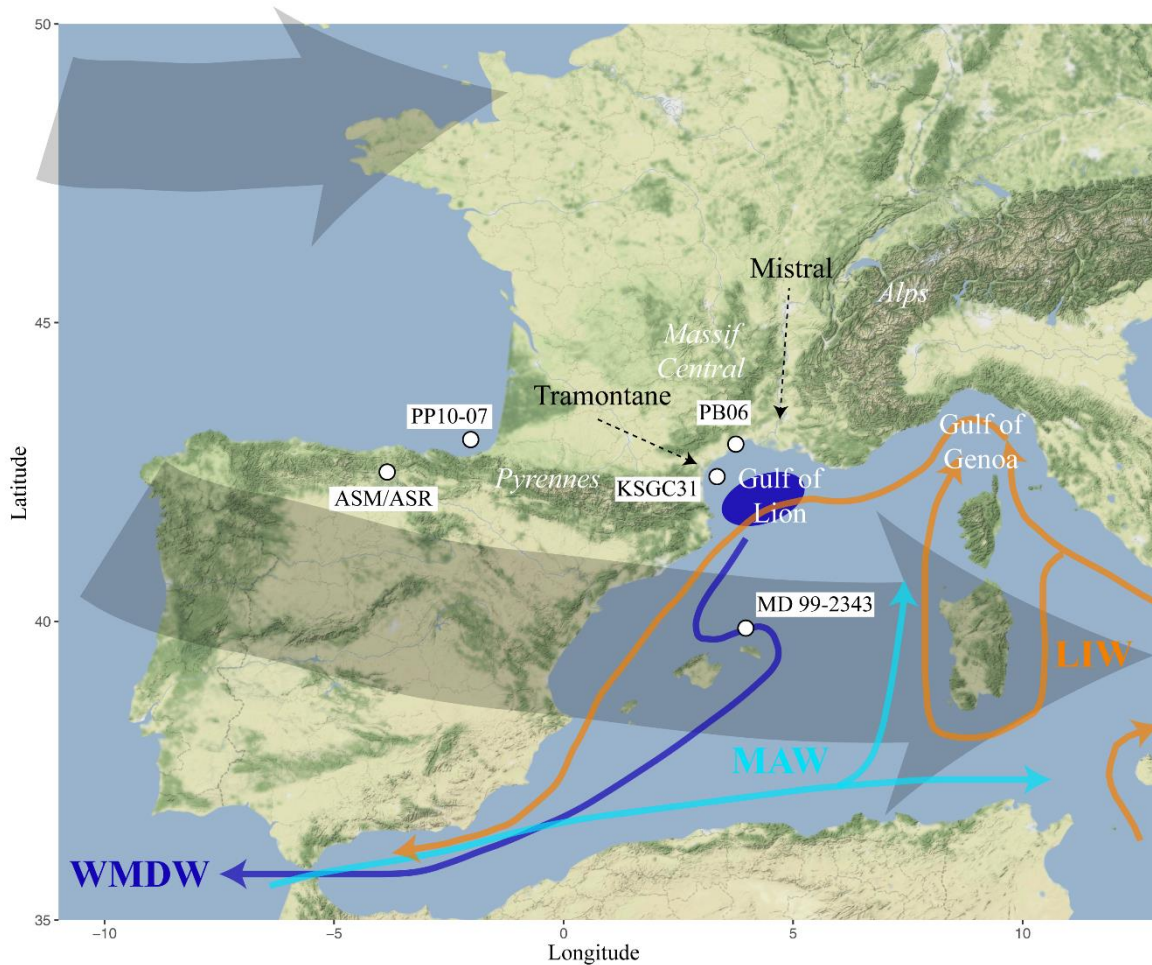
143 Mediterranean storms cyclones (e.g. Trigo and DaCamara 2000, Nissen et al. 2010, Toreti et al. 2010)
144 (Figure 1).

145 The complex orography of the northwestern Mediterranean basin and the interactions between the
146 hinterland and the Mediterranean Sea promote mesoscale convective systems and greatly contribute to
147 the regional climate specifics of this area. The Mediterranean Sea represents an important source of heat
148 and moisture (Winschall et al. 2014). Warm and humid air advection from the Mediterranean towards
149 the upland areas surrounding the Gulf of Lion causes significant rainfall and sometimes leads to HPE,
150 such as that which occurred in the Gard on the 8-9 September 2002, when 600mm of rain fell in 24
151 hours (Nuissier et al 2011). The Gulf of Genoa is one of the major cyclogenesis regions of the whole
152 Mediterranean basin and one of the most persistent throughout the year (Figure 1). The Gulf of Lion and
153 the Balearic Islands, which are situated a few hundred kilometers to the west, are secondary centers of
154 cyclogenesis linked to this very active and persistent center (Trigo et al. 1999, Lionello et al. 2016).
155 Moreover, mesoscale cyclones formed in the Gulf of Genoa promote Mistral and Tramontane winds
156 over the Gulf of Lion (Lebeaupin Brossier and Drobinski 2009).

157 Inter-annual climate variability in the western Mediterranean is greatly influenced by major patterns of
158 atmospheric variability defined by differences in seasonal average sea-level pressures (SLP) at chosen
159 locations. One of the most important is the North Atlantic Oscillation pattern (NAO) which involves
160 inter-annual differences in the seasonal mean SLP between the Azores high and the Icelandic low
161 (Hurrell et al. 2003). This pattern of variability is thus related to the strength of the meridional pressure
162 gradient along the North Atlantic sector. A positive (negative) NAO index implies a higher (or lower)
163 meridional pressure gradient which caused stronger (or weaker) westerlies. NAO variability has a
164 considerable influence on the activity of the North Atlantic storm track during winter time (Rogers 1997,
165 Hurrell et al. 2003). As a consequence, winter precipitation in the western-Mediterranean basin is higher
166 and cyclogenesis is more pronounced during negative NAO years. The Mediterranean Oscillation
167 pattern, involving contrasting pressure conditions between the western and the eastern Mediterranean,
168 is a regional manifestation of the NAO (Conte et al. 1989). In addition, the Western Mediterranean
169 Oscillation index (WeMOi), defined as the difference in pressure values between the Azores high and
170 the Ligurian low systems, has been shown to detect variability in cyclogenesis in the western
171 Mediterranean basin and thus is more effective than NAO for explaining seasonal precipitation in this
172 area, especially on the east margin of the Iberian Peninsula (Martin-Vide and Lopez-Bustins 2006). The
173 Scandinavian pattern (SCAND) is another important mode of inter-annual variability in the northern
174 hemisphere, influencing the climate of the western Mediterranean region. It is defined as the SLP
175 differences between Scandinavia and both Western Europe and Mongolia. Strong persistent positive
176 pressure anomalies over Scandinavia cause enhanced precipitation in the central and western
177 Mediterranean (Bueh and Nakamura 2007). Finally, the El Niño Southern Oscillation (ENSO), which
178 affects the tropical Pacific and Indian oceans, also impacts upon the European climate including that of
179 the western Mediterranean area (Brönnimann et al. 2007). In winter, El Niño events can induce an

180 atmospheric circulation pattern resembling a negative NAO, increasing winter precipitation rates in the
181 western Mediterranean, but with sea level pressure anomalies shifted north-eastward. On the other hand,
182 la Niña events can lead to a quasi-symmetric response, decreasing winter precipitation in the western
183 Mediterranean (Brönnimann et al. 2007). In contrast, in Spring, El Niño events may induce a contrasting
184 pattern characterized by dryer conditions in the western Mediterranean and wetter conditions in the area
185 stretching from north-western Europe to the north western Iberian Peninsula; the opposite occurs during
186 la Niña events. Nevertheless, it must be noted that these typical responses of European climate to ENSO
187 are not always well recorded (Brönnimann et al. 2007). The ENSO signal in Europe is rather non-
188 stationary and further work is needed to better characterize its modulating factors especially on decadal
189 and multidecadal time-scales (Brönnimann et al. 2007).

190 Furthermore, the Gulf of Lion is one of the few areas where deep water formation occurs in the
191 Mediterranean basin (MEDOC group 1970, Ulses et al. 2008, Frigola et al. 2007). Mediterranean waters
192 are stratified in three different layers, i.e. surface, intermediate and deep waters. The surface waters (0-
193 200m) originate in the Atlantic and flow eastwards through the Strait of Gibraltar becoming
194 progressively warmer and saltier (Modified Atlantic Waters, MAW) (Figure 1). The intermediate waters
195 (200-500m) form in the eastern Mediterranean during the winter season when dry, cold air from Anatolia
196 causes surface waters to sink (Levantine Intermediate Waters, LIW) (Figure 1). Finally, the deep waters
197 (>500m) form in the northern part of the Mediterranean basin where MAW is cooled by winds and
198 mixed with LIW until they reach bottom water density and sink towards the abyssal plains (Western
199 Mediterranean Deep Water, WMDW) (Rhein 1995, Schroeder et al. 2010). In the Gulf of Lion, the dry
200 and cold Mistral and Tramontane winds are responsible for deep water formation (Figure 1). The Mistral
201 blows from the north following the Rhône valley while the Tramontane blows from the northwest
202 through the plain between the Pyrenees and the Massif Central. They both cause surface water heat loss
203 within the gulf and thus lead to relatively low SST compared to the rest of the Mediterranean basin
204 (Sicre et al. 2016). In summary, the climate of the Gulf of Lion results from the complex interactions
205 between remotely driven processes and local features.



206
 207 *Figure 1: Locations of studied core sequences. Thin colored arrows represent marine currents (MAW,*
 208 *Modified Atlantic Waters; WMDW, Western Mediterranean Deep Waters; LIW, Levantine Intermediate*
 209 *Waters), black dotted arrows represent winds of southern France, and large shaded grey arrows*
 210 *represent the southern part of the Atlantic storm track. The blue oval represents the zone of formation*
 211 *of Western Mediterranean Deep Waters (WMDW).*

212 **Methods**

213 The aim of this article is to compare paleoclimatic time series in the frequency domain in order to
 214 identify similar patterns of variability and to draw connections between distinct climate proxies. To this
 215 end, we used spectral analysis methods specifically adapted to deal with irregularly sampled time series,
 216 as the resampling with constant time-steps can introduce unpredictable biases in the results (Schulz and
 217 Stattegger 1997, Schulz and Mudelsee 2002, Witt and Schumann 2005, Pardo-Igúzquiza and Rodríguez-
 218 Tovar 2012, Polanco-Martínez and Faria 2018, Lenoir and Crucifix 2018a and b). Given the importance
 219 of non-stationarities to understand Holocene climate variability (Witt and Schumann 2005) we chose to
 220 analyze the data selected for this work using wavelet spectral analysis for unevenly sampled time series
 221 (Lenoir and Crucifix 2018b). Wavelet spectral analyses are designed to deal with non-stationary time
 222 series that allow us to determine the dominant modes of variability embedded in a signal and how these

223 modes vary over time (Torrence and Compo 1998). On the other hand, the results of wavelet spectral
224 analysis can display false dominant periodicities, especially for the lower frequencies that are of
225 particular interest to us (Hochman et al. 2019). Thus, we chose to also use an univariate spectral analysis
226 method for irregularly sampled time series developed by Schulz and Stattegger (1997) and Schulz and
227 Mudelsee (2002) which, unlike wavelets, does not allow one to detect non-stationarities, but allows one
228 to check whether the significant low frequency features detected in wavelet spectral analyses are actually
229 present in the signal or not.

230 The central assumption of this work is that, if two signals share statistically significant features in the
231 time/frequency space, they may be linked in some way; we review the mechanisms which could explain
232 such a link. It is important to note that wavelet spectral analysis allows to characterize pseudo-periodic
233 and non-periodic oscillations just as well as fully periodic oscillations. Here, we are looking for
234 significant shared features in the wavelet spectra of the studied paleoclimatic time series; these features
235 can highlight connections between spectra regardless of whether they are periodic or pseudo-periodic.

236 Wavelet spectral analysis, generalities

237 Wavelets are small wave functions with zero mean, localized in both the time and frequency domains.
238 This means that they rapidly approach zero after few oscillations in the time domain and they display
239 narrow-bandpass-like spectra in the frequency domain (admissibility conditions, Farge 1992, Torrence
240 and Compo 1998). Wavelet function also need to have a number of oscillations that remain constant
241 when they are translated or dilated, which makes it possible to generate from a single mother wavelet
242 similar wavelet functions (daughter wavelets) that differ only in their localization in time and the
243 frequency on which their Fourier transform is centered (similarity condition, Farge 1992). Therefore, a
244 daughter wavelet is characterized by a non-dimensional time index (τ) quantifying its translation along
245 the time axis and a scale (a) indicating the factor by which it has been dilated relatively to the mother
246 wavelet.

247 The convolution of a time series with a daughter wavelet characterized by a given τ and a allows to
248 investigate the contribution of a given frequency (related to the scale a by a formula depending on the
249 mother wavelet) to the variability of the signal around the time τ ; this is the continuous wavelet
250 transform. By varying the scale and the time index, wavelet transforms allow to examine the contribution
251 of a set of frequencies to the signal variability along the time series; this is why wavelet analyses are
252 called “time/frequency analyses.” The results of such analyses are presented in the form of a scalogram,
253 a graph with time in abscissa, scales or corresponding frequency or periods in ordinate, and the wavelet
254 power (the square modulus of the wavelet transform) color coded. A periodic or pseudo-periodic feature
255 of period λ that contributes to signal variability within the time interval $[t_1, t_2]$ is characterized by a
256 power local maximum centered on λ between t_1 and t_2 .

257 In this article, wavelets derived from the Morlet mother wavelet are used:

258

$$\psi_0(\eta) = \pi^{-1/4} e^{i\omega_0\eta} e^{-\eta^2/2}$$

259

260

261

262

263

264

265

266

267

268

269

270

271

272

273

The input η is a non-dimensional time parameter and ω_0 is the non-dimensional frequency, here equal to 5.5 in order to have the finest time resolution while satisfying the admissibility conditions (see Lenoir and Crucifix 2018b). The Morlet wavelet is a complex plane wave modulated by a gaussian. It is a nonorthogonal wavelet function better adapted to time series analysis than orthogonal wavelet functions because it is highly redundant at large scales so is more appropriate to catch smooth and continuous variations in wavelet amplitude. Moreover, as it is a complex function, the Morlet wavelet transform can be divided into a real and an imaginary part, which gives information about both amplitude and phase. The Morlet wavelet transform thus allows to better characterize oscillatory behavior in the analyzed time series than real wavelet functions, which are more useful for identifying isolated peaks and discontinuities. Finally, the Morlet wavelet is relatively wide compared to other complex nonorthogonal wavelets such as the Paul wavelet, which results in a lower resolution in terms of time but a better frequency resolution (Torrence and Compo 1998). Morlet wavelets are widely used for paleoclimatic time series analysis and more generally for geophysical and ecological data (i.e. Cazelles et al. 2008, Torrence and Webster 1999).

Wavelet spectral analysis of irregularly sampled time series

274

The scalogram under the formalism of orthogonal projection

275

276

277

278

279

280

281

282

283

284

285

286

287

288

289

290

291

292

293

In this study, wavelet spectral analyses are performed with the algorithm developed by Lenoir and Crucifix (2018b) which is a generalization of Foster's (1996) pioneering work, used by Witt and Schumann (2005) to analyze paleoclimatic time series in Greenland. However, it includes more sophisticated significance testing, scalogram smoothing and takes into account aliasing issues (Lenoir and Crucifix 2018b). The main particularity of Foster (1996) and Lenoir and Crucifix (2018b) is to perform wavelet spectral analysis under the formalism of orthogonal projections. Unlike classical methods that define the continuous wavelet transform as the convolution product of a time series with a wavelet function, they define the continuous wavelet transform as an orthogonal projection on a vector space. In this approach, a time series X of length N is represented by two vectors of length N : the vector representing the measures $|X\rangle$ and a vector representing the times $|t\rangle$ at which the measures were made. The wavelet transform of X is the projection of the vector $|X\rangle$ onto a vector space spanned by two linearly independent vectors (a plane), $G_{\tau,a}\cos(|t\rangle/a)$ and $G_{\tau,a}\sin(|t\rangle/a)$, which are the scaled sine and cosine of the time vector $|t\rangle$ multiplied by a gaussian taper ($G_{\tau,a}$) varying with both time index and scale. The result of such a projection is a vector of length 2 whose components are its coordinates in the plane defined by the basis $\{G_{\tau,a}\cos(|t\rangle/a), G_{\tau,a}\sin(|t\rangle/a)\}$ and are analogous to the real and the imaginary part of the classical wavelet transform. The wavelet power plotted in the scalogram is simply the squared norm of this vector. Under this formalism, the wavelet transform gives very similar results to the classical approach and can easily be applied to irregularly sampled time series. Moreover, it is possible to define an orthogonal projection that is invariant with respect to the mean and

294 the trend of a time series, allowing one to compute the wavelet transform and the scalogram without any
295 preprocessing of the data.

296 *The weighted smoothed scalogram*

297 In spectral analysis, the data analyzed can be modeled by a periodic signal—a cosine or sine wave
298 characterized by a frequency and an amplitude—with a long-term trend and noise superimposed on it.
299 Under this assumption, a way to perform time/frequency analysis is to determine for a given time and
300 a given frequency the amplitude characterizing this periodic component. If a frequency contributes
301 strongly to the total variability of the signal at a given time, this will correspond to a strong amplitude
302 for the periodic component, whereas if a frequency is absent, this will result in a zero amplitude. The
303 result of such analysis is called the amplitude scalogram and is approximately proportional to the
304 scalogram defined in the previous paragraph. It follows that, from a computational point of view, a
305 convenient way to study how the amplitude of the periodic component varies in the time/frequency
306 plane is to weight the scalogram by a factor related to the gaussian tapper $G_{\tau,a}$; this is the weighted
307 scalogram.

308 Another issue is that the scalogram obtained from the analysis of a time series is not a consistent
309 estimator of the true frequency content of the studied process. This means that the scalogram is just an
310 estimation of the frequency content of the sampled signal varying with time, and, more importantly,
311 that the error of this estimation does not converge to zero when the number of data points increase.
312 From a practical point of view, this implies that the scalogram will remain noisy regardless of the
313 quality of the data. In order to fix this problem, the scalogram needs to be smoothed. A weighted
314 scalogram is smoothed over time by averaging the points of same scale (a) around a given time index
315 (τ) within the time window $[\tau - \gamma\omega_0 a, \tau + \gamma\omega_0 a]$, with γ as the smoothing coefficient. Lenoir and
316 Crucifix (2018b) recommend the use of the weighted smoothed scalogram in most time-frequency
317 analyses of irregularly sampled time series; we thus use it in this article to analyze the studied
318 paleoclimatic sequences.

319 *Practical considerations*

320 We used the WAVEPAL python package (<https://github.com/guillaumelenoir/WAVEPAL>), which
321 allows time-frequency analysis of irregularly sampled time series using the weighted smoothed
322 scalogram (Lenoir and Crucifix 2018b). The temporal resolution of the weighted smoothed scalogram,
323 i.e. the number of time indices at which it is calculated, is equal to the length of the analyzed time series
324 to avoid oversampling. For each time series, a polynomial trend is fitted by visual inspection. Even if
325 the time series is not detrended, the degree of this polynomial trend is necessary to defined an orthogonal
326 projection invariant with respect to this trend. The degrees of the polynomial trends fitted to the studied
327 proxies are given in the Table 1. The smoothing coefficient $\gamma = 0.5$ was chosen for all sequences, and
328 the length of integration was kept constant for a given scale when the smoothing interval intersected the
329 edge of the time/frequency plane, meaning that parts of it were excluded from the analysis. One way to

330 quantify the degree of smoothing is to use a scale independent index—in the case of smoothing over
331 time (Maraun and Kurths 2004), the length of the time windows divided by the scale ($m = 2\gamma\omega_0$).
332 Regarding this criterion, a smoothing coefficient of $\gamma = 0.5$ corresponds to a relatively high degree of
333 smoothing ($m = 5.5$, Maraun and Kurths 2004). On the other hand, since the length of the smoothing
334 time window depends on the scale, it implies that the smoothing will have little or no effect on smaller
335 scales, since the smoothing time interval will contain only one or very few points to be averaged. Thus,
336 for each of the time series, we give the period for which the smoothing interval contains at least 4 points
337 (Table 1) and we call it the “minimum consistent period”. For time series with large time steps (~50 yrs)
338 one possibility would have been to increase the degree of smoothing by taking a higher smoothing
339 coefficient; however such a choice would dramatically reduce the temporal resolution of the larger scales
340 and for the present work, these larger scales are of more interest than small scales, considering the
341 uncertainties of the age models of the studied time series (see below). Finally, for all time series, we
342 used a coefficient of scale resolution equal to $\delta j = 0.05$, which is the largest value that gives an adequate
343 sampling in scale for the Morlet wavelet (Torrence and Compo 1998). A smaller δj could have been
344 used in order to have a finer resolution, but such a resolution would increase the time of the analysis,
345 which can be a problem when quantifying the uncertainty due to age models (see below) without visibly
346 improving the results.

347 Significance testing

348 The significance of the highlighted features in the time/frequency plane was statistically tested with
349 hypothesis testing using the WAVEPAL and CARMA (https://github.com/brandonckelly/carma_pack)
350 python packages. For each point of the time/frequency plane, we independently tested the null-
351 hypothesis (H_0) that there is no periodic component in the analyzed signal for a given scale (i.e.
352 frequency) and time index pair. To this end, the distribution of each point of the weighted smoothed
353 scalogram was calculated under the null-hypothesis and the points of the data scalogram above the X^{th}
354 percentile were considered to be significant with a (100-X)% level of significance, entailing a rejection
355 of the null-hypothesis with X% confidence (Lenoir and Crucifix 2018b). For all analyses, the 5 and 10%
356 confidence levels were plotted on the scalograms.

357 A crucial step for this significance testing is to correctly estimate the distribution of points on the
358 scalogram under the null hypothesis, derived analytically (Lenoir and Crucifix 1998). Under the null
359 hypothesis, the analyzed time series is considered to be a trend with background noise superimposed on
360 it, so the characteristics of this noise are crucial to derive reliable distributions. In Lenoir and Crucifix
361 (2018), the background noise is modeled by a zero-mean stationary Gaussian CARMA (Continuous
362 Autoregressive Moving Average) process, sampled at the times $|t >$ of the time series. CARMA
363 processes are a way to model stochastic processes in continuous time in order to have a better
364 representation of underlying physical processes which are actually continuous. This allows to work
365 easily with irregularly sampled time series (Kelly et al. 2009, 2014) compared to discrete autoregressive

366 process commonly used when working with regularly sampled data (Torrence and Compo 1998).
367 CARMA (p, q) processes are characterized by their order p and q , which represent the number of terms
368 in the left and right part of the model's stochastic differential equation. In practice, only CARMA
369 processes of low order are useful in the context of spectral analysis since high order CARMA processes
370 can display dominant spectral peaks even when they are purely random. A CARMA (0,0) process is
371 equivalent to white noise, i.e. a random process normally distributed. A CARMA (1,0) process is
372 equivalent to a continuous first-order autoregressive process (also called a Ornstein-Uhlenbeck process)
373 which is the continuous-time analog (Kelly et al. 2009, 2014) of the widely used first-order
374 autoregressive process (AR1) for significance testing in spectral analysis (e.g. Torrence and Compo
375 1998, Schulz and Mudelsee 2002).

376 In this article we choose to use a CARMA (1,0) process as background noise for the significance testing.
377 Indeed, spectra of paleoclimatic time series often display a decreasing spectral amplitude with increasing
378 frequency, which can be explained simply by a random AR(1) process (Hasselmann 1976, Schulz and
379 Mudelsee 2002). Assuming that the studied time series is a just trend with a CARMA(1,0) process
380 superimposed on it (null-hypothesis), the trend is removed and the CARMA python package is used to
381 estimates the characteristics of this noise. The WAVEPAL package is then able to analytically compute
382 the distribution of the scalogram points and the corresponding confidence level from the previous
383 results.

384 Edge effects and aliasing issues

385 In classical wavelet spectral analysis of regular sampled time series using the convolution function
386 method, errors are likely to appear at the margins of the scalogram because the time series analyzed are
387 of finite length and the use of the Fourier transform assumes the data is cyclic (Torrence and Compo
388 1998, Zhang and Moore 2011). One way to solve this problem is to pad the end of the time series with
389 zeros before performing the wavelet transform; however, this zero-padding will decrease the amplitude
390 of the result near the edge of the time/frequency plane. This is why a “cone of influence” is usually
391 plotted on a scalogram to visualize where such edge effects become important and cannot be neglected
392 (Torrence and Compo 1998, Zhang and Moore 2011). Under the formalism of orthogonal projections,
393 Fourier transforms are not used so there is no need for zero-padding, but this doesn't mean that there are
394 no edge effects in the scalogram. Indeed, near the edge of the time series, in areas in which length
395 increases with the scale, part of the wavelet supports can stand outside bounds of the data (Lenoir and
396 Crucifix 2018b). This implies that, in these parts of time/frequency plane, the small waves of the
397 $G_{\tau,a} \cos(|t >/a)$ and $G_{\tau,a} \sin(|t >/a)$ vectors on which the data vector $|X >$ is projected are truncated
398 at one end as they approach zero, which can of course affect the results of the analysis. For this reason,
399 a “cone of influence” is also defined under the formalism of orthogonal projection for those regions
400 where edge effects are not negligible (Lenoir and Crucifix 2018b). The length of this “cone of influence”
401 on each side of the time/frequency plane is proportional to the width of the wavelet and is given by the

402 formula $\sqrt{2}\omega_0 a$ (Torrence and Compo 1998, Lenoir and Crucifix 2018b). The “cone of influence”
403 corresponds to the shaded grey area on both sides of the scalograms.

404 In the case of irregularly sampled time-series, the scale of the wavelet packet may be too low compared
405 to the local time step, leading to the erroneous detection of high frequency periodicities which are not
406 present in the signal. This bias, called aliasing, can be prevented by excluding from analysis some areas
407 of the time-scale plane (Lenoir and Crucifix 2018b). These excluded areas form the Shannon-Nyquist
408 exclusion zone (SNEZ), with reference to the Shannon-Nyquist sampling theorem from which they are
409 calculated. The SNEZ is represented in black at the bottom of the scalograms. Due to correlation
410 between neighboring scales and to smoothing in the scalogram, the SNEZ must be slightly extended
411 (Lenoir and Crucifix 2018b). In the scalograms, this extension of the SNEZ is the shaded grey area just
412 above the SNEZ.

413 Finally, according to a recommendation in Lenoir and Crucifix (2018b), we chose a fixed length of
414 integration when computing the weighted smoothed scalogram. This resulted in two more excluded
415 areas in black at the right and the left of the scalogram.

416 Propagation of age model uncertainties in wavelet spectral analysis

417 Most paleoclimatic sequence chronologies are based on radionuclide measurements and are therefore
418 affected by age model uncertainties. These uncertainties introduce an inherent bias within all types of
419 spectral analysis (Mudelsee et al. 2009, Rhines and Huybers 2011). In most of the papers dealing with
420 spectral analysis of paleoclimatic sequences this problem is not considered and not even mentioned,
421 despite the fact that it can affect both the significance of a spectral peak and the estimation of its position
422 (Mudelsee et al. 2009). Even if there is no way to avoid this bias, it is possible to quantify it. For this
423 study, a short program based on a Monte Carlo method was written with Python to propagate age model
424 errors within wavelet spectral analysis and to estimate their effect on the position of the scalogram
425 maxima along the scale (period) axis. Such a method for propagating age model uncertainties has been
426 used previously by Anchukaitis and Tierney (2013) to conduct an empirical orthogonal function analysis
427 on proxies from different sequences.

428 First, the age models of all the studied time series were recalculated from scratch with the RBACON R
429 package for age-depth modeling using Bayesian statistics (Blaauw and Christen 2011,
430 <https://CRAN.R-project.org/package=rbacon>). At the same time, 3000 alternative age models without
431 age reversals were generated with RBACON for each time series using the same method. The most
432 straightforward way to address the issue of age model error would have been to use these alternative
433 age models to compute 3000 alternative weighted smoothed scalograms for each time series. This
434 would have allowed an easy evaluation of the impact of the age model uncertainties on each point of
435 the time/frequency plane. However, this is not practical due to the computation time required to
436 calculate a single weighted smoothed scalogram (several minutes for most of the time series studied
437 here), resulting in an algorithm requiring several days to perform a single analysis. Thus, we decided

438 to characterize the significant features of our scalograms by looking at the position of local maxima in
439 scalogram “slices” along the period axis and propagate the age model uncertainties only for these
440 selected slices. The positions of local maxima observed in a scalogram may of course vary with the
441 time indices of the chosen slices; nevertheless, maxima positions will vary very gradually as the
442 adjacent points of a scalogram are highly correlated along the time axis (Maraun and Kurth 2004).
443 Let’s take an example to see how the algorithm works. Let’s consider a time series call X with $|X >$
444 the vector of its measures and $|t >$ the vector of its sampling times. A simple visual observation
445 reveals that the weighted smoothed scalogram of X displays a significant local maximum between
446 $[t_1, t_2]$ at a period around λ_{obs} (The WAVEPAL python package allows horizontal dashed lines to be
447 drawn across the scalogram, which is convenient for approximating periods). In order to evaluate the
448 consequences of age model errors on the period characterizing this maximum we use the following
449 procedure:

- 450 • A time t_{obs} , with $t_1 < t_{obs} < t_2$, is chosen by visual observation where the local maximum
451 around λ_{obs} is particularly well marked
- 452 • The program will calculate the exact period λ_{calc} of this local maximum for the time index
453 $t_{calc} \in |t >$ closest to t_{obs} .
- 454 • Then 3000 scalogram slices for this time index t_{calc} will be calculated with exactly the same
455 parameters but 3000 different time vectors $|t >$.
- 456 • The program will then search in each of these 3000 scalogram slices for the alternative local
457 maximum $\lambda_{alt,i}$ closest to the reference value λ_{calc} to obtain 3000 possible period values.
- 458 • Finally, 5th and 95th quantiles of the 3000 $\lambda_{alt,i}$ distribution will be used to define an interval
459 within which the true period will theoretically have a 90% chance of being found.

460 This method allows us to address the influence of age model uncertainties on period estimates in a
461 rapid and straightforward way. On the other hand, for computational practicality, we were obliged to
462 compute the 3000 alternative scalogram slices without smoothing. As mentioned above, the
463 unsmoothed scalogram is not a consistent estimator of the frequency content; nevertheless, this does
464 not appear to be a major problem in this particular case. Before each analysis, we compared, for the
465 chosen time index, the period of the local maximum obtained with the smoothed and unsmoothed
466 weighted scalograms in order to assess the discrepancy between the two. In most cases the values
467 found were strictly identical, and when they were not, they remained extremely close (Appendix 1,
468 Table I). As already mentioned, adjacent points of the raw scalogram are highly correlated along the
469 time axis (Maraun and Kurths 2004) and the smoothing performed mostly affects the absolute value of
470 the local maxima in the scalogram and not their position along the period axis.

471 Welch's Overlapped Segment Averaging method

472 The REDFIT program (Schulz and Mudelsee 2002) was used to re-analyze all the paleoclimatic time
473 series using an independent method of spectral analysis in order to check the reliability of low
474 frequency features detected with wavelet spectral analyses. The algorithm of the REDFIT program is
475 based on the Lomb-Scargle Fourier transform (Lomb 1976, Scargle 1982) and Welch's Overlapped
476 Segment Averaging procedure (Welch 1967, WOSA method). Just as for the raw wavelet scalogram,
477 the raw auto-spectrum of a time series obtained from the Lomb-Scargle Fourier transform is not a
478 consistent estimator of its true frequency content—it needs to be smoothed. Thus, the time series is
479 divided into several segments with 50% overlap. A linear trend is subtracted from each segment to
480 avoid biases at low frequencies. Then, each segment is multiplied by a chosen taper to reduce spectral
481 leakage. Finally, the auto-spectrum (periodogram) of the time series is calculated as the average of the
482 Lomb-Scargle Fourier transforms of all the detrended and tapered segments (Schulz and Stattegger
483 1997, Schulz and Mudelsee 2002).

484 In practice, we used the Welch taper for most of our analyses (Welch 1967). Tests realized using other
485 available tapers in the REDFIT program gave us equivalent results. On the other hand, the number of
486 segments is a key parameter of this method. For a time series with a given number of points, a larger
487 number of segments will reduce the noise in the auto-spectrum but also decrease the frequency
488 resolution, reducing at the same time the minimum frequency (i.e. the maximum period) that can be
489 investigated. Since we are particularly interested in low frequencies (long periods), we used relatively
490 small numbers of segments (between 3 and 5) which in each case allowed us to obtain information on
491 periods up to 2000 years while maintaining a satisfactory degree of smoothing. These numbers of
492 segments are consistent with those found in the bibliography for time series with numbers of points of
493 the same order of magnitude as those studied here (e.g. Oppenheim et al. 1999, Schulz and Mudelsee
494 2002). The results of these analyses are referred to in the Discussion, and are presented in detail in
495 Appendix 1.

496 Comparison of time series in the frequency domain

497 To compare time series in the frequency domain, methods of cross-spectral analysis with statistical
498 tests of significance must be used. Wavelet coherency analysis would have been ideal (Maraun and
499 Kurths 2004), but this method is not implemented in the WAVEPAL python package and, to best of
500 our knowledge, has not yet been adapted for irregularly sampled time series. We thus decided to use
501 the program REDFIT-X for cross-spectral analysis of unevenly spaced paleoclimate time series (Björg
502 Ólafsdóttir et al. 2016) which generates a coherency spectrum based on the WOSA method (see
503 paragraph above).

504 The coherency of two time series x and y is defined as the squared modulus of their cross-spectrum
505 (G_{xy}) normalized by the product of their auto-spectrum (G_{xx}) and (G_{yy}). The cross-spectrum is
506 computed using the WOSA method. The time series are divided into overlapping segments which are

507 detrended and tapered. Then a “local” cross-spectrum ($G_{xy,i}$) is calculated for each segment i as the
 508 product of the Lomb-Scargle Fourier transform of one time series (X_i) with the complex conjugate of
 509 the Lomb-Scargle Fourier transform of the second one (Y_i^*) for the same segment:

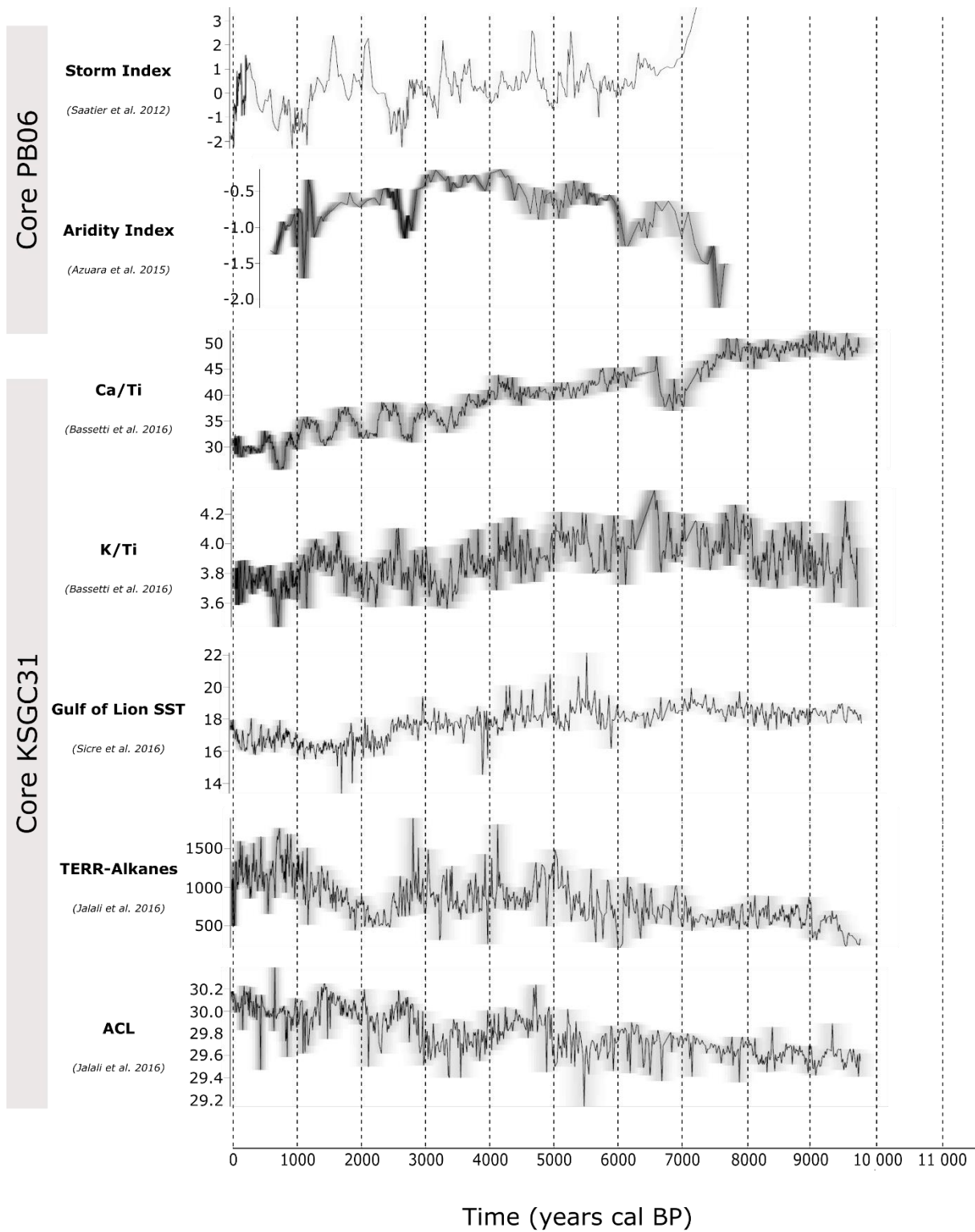
$$510 \quad G_{xy,i}(f) = X_i(f)Y_i^*(f)$$

511 The coherency spectrum is obtained by averaging all the local cross-spectra. It is a dimensionless
 512 measure of the degree of linear relationship between two time series in the frequency domain which
 513 range from 0 (no relationship) to 1 (perfect relationship). In practice, coherency is corrected to obtain a
 514 bias-corrected coherency spectrum, since for a given frequency, the raw spectrum is greater than zero
 515 even for uncorrelated time series. This bias-corrected coherency spectrum is calculated for frequencies
 516 in the range from the fundamental frequency ($f_{fund,xy}$) to the average Nyquist frequency ($f_{Nyq,xy}$)
 517 which are obtained from the time series with the lower resolution, thus $f_{fund,xy} =$
 518 $max(f_{fund,x}, f_{fund,y})$ and $f_{fund,xy} = min(f_{Nyq,x}, f_{Nyq,y})$.

519 Finally, it is important to note that, because the REDFIT-X program is based on the WOSA method, it
 520 therefore assumes that the analyzed signals are stationary, which is obviously not the case for our
 521 selected paleoclimatic time series in light of the results of the wavelet spectral analyses (see Results
 522 and Discussion). It is thus possible that non-stationary spectral features with close periods and time
 523 ranges that are detected in different time series using wavelets may not appear in the cross-spectral
 524 analyses using REDFIT-X.

Time series	Number of samples	Minimum time (yrs cal BP)	Maximum time (yrs cal BP)	Mean time steps (yrs)	Age control	Mean age models error (years)	Minimum consistent period (years)	Degree of the polynomial trend
Aridity Index	127	585	7719	56.17	28 ¹⁴ C dates and 5 historical dates	± 135	256	2
Storm Index	370	-55	7333	19.96	28 ¹⁴ C dates and 5 historical dates	± 135	91	5
Ca/Ti	654	41	9731	14.81	20 ¹⁴ C dates	± 211	68	3
K/Ti	654	41	9731	14.81	20 ¹⁴ C dates	± 211	68	1
Gulf of Lion SST	690	-17	9770	14.18	20 ¹⁴ C dates	± 211	65	4
ACL	681	-17	9760	14.35	20 ¹⁴ C dates	± 211	66	3
TERR-Alkanes	681	-17	9760	14.35	20 ¹⁴ C dates	± 211	66	3
Bay of Biscay SST	206	445	10195	47.33	10 ¹⁴ C dates	± 302	216	6
δ ¹⁸ O of cave Speleothem	513	13	7783	15.14	22 U/Th	NA	69	2
ENSO variability	12301	0	11499	0.93	See Publication	NA	4	2

525 Table 1: General information about the analyzed time series, NA means that the value is not available.



526

527 *Figure 2: Curves of the studied time series. Shaded grey area represent the age models errors of each*
 528 *time series plotted using the “proxy.ghost” function of the RBACON package, darker grey indicate*
 529 *more likely ages for specific proxy values.*

530

531 **Data sets and results**

532 This section summarizes the context, the chronological framework and the meaning of the climate
533 proxies used in this study; it also describes briefly their main features in the frequency domain. The
534 original curves of the Gulf of Lion sequences are presented in Figure 2 and the general characteristics
535 of all time series are given in the Table 1 (Number of samples, length, mean time step, age control, mean
536 age model error, minimum consistent period and degree of the polynomial trend). The detailed results
537 of the age models error propagation are presented in a table in the Appendix 1.

538 PB06 core and the Palavasian lagoon system

539 The Palavasian lagoon system is located in southern France (Figure 1) along the coast of the Gulf of
540 Lion. The wetland complex consists of seven shallow ponds (depth <1m) (Sabatier et al., 2008). These
541 hypersaline, back-barrier lagoons are separated from the Mediterranean Sea by a wave-produced, sandy
542 barrier measuring 150 m wide and rising to a height of 2–3m above the mean sea level. Tidal variability
543 is modest (with a mean range of 0.30 m), which minimizes the influence of dynamic tidal currents. The
544 study site is located along the southeastern-facing shoreline and is extremely vulnerable to intense
545 storms blowing from the south and southeast (Dezileau et al. 2011).

546 A 7.9 m long core (PB06) was recovered from Pierre Blanche Pond in 2006 (Dezileau et al. 2011,
547 Sabatier et al. 2010, 2012). The chronology was established using 25 Accelerator Mass spectrometry
548 (AMS) radiocarbon dates on monospecific shell samples of *Cerastoderma glaucum*. The radiocarbon
549 reservoir ages were estimated in relation to historical events and paleoenvironmental changes (Sabatier
550 et al. 2010b). For the last centuries, historical storm events, together with short-lived radionuclide
551 measurements, were also used (Sabatier et al. 2012).

552 *Sedimentological analysis*

553 Several analyses were performed on core PB06. Clay minerals were identified and quantified by X-ray
554 diffraction (XRD) and X-ray fluorescence analyses (XRF) were also performed to estimate Al, Si, S, Cl,
555 K, Ca, Ti, Mn, Fe, Zn, Br, Sr, Rb, and Zr contents (Sabatier et al. 2012). The macrofauna content was
556 estimated by sieving samples at 1mm and identifying the shells every 2cm in order to identify lagoonal
557 and marine species (Sabatier et al. 2012).

558 Storms are frequent in the northern Mediterranean during the wet season (October to March) and the
559 most powerful ones are able to break the sandy barriers of coastal lagoons causing marine sediments to
560 enter the ponds and creating what are called overwash fans as illustrated in Sabatier et al. (2008). Thus,
561 sedimentological archives from coastal lagoons potentially represent long term records of past intense
562 storms. Distal overwash fans are clearly identified in PB06 through the presence of marine mollusk
563 shells (M), changes in clay mineralogy (C) and increases in the Zr/Al ratio (Z). On the basis of this
564 sedimentological evidence, several periods of intense storm activity have been defined (Figure 2)
565 (Sabatier et al. 2012). For the purpose of this study, all of these indicators of past storm activity were
566 combined to sum up all of the information within one unique time series called the “Storm Index” (SI):

567
$$SI(t) = -C(t) + 3 \times \frac{M(t)}{\max(M)} + 3 \times \frac{Z(t)}{\max(Z)}$$

568 The M and Z time series are scaled by dividing them by their maxima, $\max(M)$ and $\max(Z)$, and then
 569 multiplying them by a factor 3 to have an amplitude of variation of about the same order of magnitude
 570 as the C time series. High SI values correspond to periods of frequent storms while low SI values
 571 correspond to periods with fewer storms.

572 The SI record from the Palavasian lagoon covers the last 7300 yrs with a mean temporal resolution of
 573 about 20 yrs (Table 1). After 4000 yrs cal BP, a major significant spectral feature of 1530-1590 yrs
 574 arises and continues until the end of the Holocene. Between 2500 and 1500 yrs cal BP, a significant
 575 spectral feature of 690-850 yrs is recorded. Finally, significant spectral features of 130-280 and 90-210
 576 are recorded at around 2500 and 5500 yrs cal BP (Figure 3).

577 *Paleoecological analysis*

578 For pollen extraction, samples were sieved, processed with HCl and HF for mineral digestion and
 579 sodium polytungstate for density separation. Pollen concentration was estimated by adding a known
 580 amount of Lycopodium spores. Pollen grains were counted and identified at 400x and 1000x
 581 amplification, respectively, with reference to pollen keys, atlases and comparison with a reference
 582 collection (Azuara et al. 2015, 2018).

583 In the French Mediterranean Mountains, *Fagus sylvatica* and *Abies alba* are at the limit of their
 584 geographical range. Thus, both taxa are particularly sensitive to climate fluctuations. Decreases
 585 (increases) in pollen proportions of these two taxa synchronous with increases (decreases) in deciduous
 586 *Quercus* proportions have been interpreted as repetitive mountainous forest retreats toward higher
 587 altitudes coinciding with repeated expansions of deciduous *Quercus* at lower altitudes during dry events
 588 (Azuara et al. 2015, 2018). The covariations of these taxa are summarized within a single indicator
 589 called “Aridity index” (A_i):

590
$$A_i = \log \left(\frac{F_p + A_p}{Q_p} \right)$$

591 F_p , A_p and Q_p are respectively *Fagus*, *Abies* and deciduous *Quercus* pollen proportions. An increase
 592 in A_i indicates increasing aridity recorded by the vegetation.

593 The aridity index time series ranges from 570 to 7800 yrs cal BP with a mean temporal resolution of
 594 about 60 yrs (Table 1). Before 5000 yrs cal BP, a significant spectral feature of 1180-1400 yrs prevails
 595 in the signal, while after 4000 yrs cal BP, a significant spectral feature of 1850-2120 yrs is rather
 596 recorded. Two significant spectral features of 430-700 yrs and 550-1140 yrs are recorded between 2000
 597 and 4000 yrs cal BP (Figure 3).

598 KSGC-31_GolHo-1B composite core and the inner shelf of the Gulf of Lion

599 The KSGC-31_GolHO-1B sequence is composed of two cores retrieved from the same site on the inner
 600 shelf of the Gulf of Lion (Bassetti et al. 2016, Jalali et al. 2016, 2017) (Figure 1). In this part of the inner

601 shelf, sediments predominantly come from the Rhône river mouth where they are advected along the
602 coast by longshore drift thereby forming the Rhône mud belt (Bassetti et al. 2016). The chronology of
603 the KSGC-31_GolHO-1B sequence is based on 20 AMS radiocarbon dates on mollusk shells and 210
604 Pb measurements. The local marine reservoir age is $\Delta R = 23 \pm 71$ years (Jalali et al. 2016, Bassetti et
605 al. 2016).

606 *XRF analysis*

607 Core KSGC-31 was split into two parts and scanned with an XRF core scanner (IFREMER) to produce
608 semi-quantitative estimates of major and minor element abundances within the sediments with a high
609 resolution, one-centimeter step measurement. The results were expressed as element to element ratios
610 and the resulting time series ranges from 110 to 10 050 yrs cal BP with a mean temporal resolution of
611 about 15 yrs (Table 1, Bassetti et al. 2016).

612 The Ca/Ti ratio is considered to record biogenic marine productivity, marked by the Calcium abundance,
613 versus terrigenous inputs, marked by the Titanium content. This proxy displays two main significant
614 spectral features of 1660-1980 yrs between 4000 and 8000 yrs cal BP and 510-700 yrs after 4000 yrs
615 cal BP, and a very short one of 170-400 yrs around 1000 yrs cal BP (Figure 3).

616 On the other hand, K/Ti values can be related to the transport of clay minerals, in particularly to the illite
617 content that forms by the weathering of K-feldspars upon pedogenetic (sub-aerial) processes. The Rhône
618 waters deliver a variable amount of illite and chlorite to the Mediterranean Sea depending on the areas
619 of its watershed that are most eroded by precipitations. Thus, illite (K) relative abundances can be used
620 as a proxy for sediments sources and indirectly of changes in rainfalls distribution. This time series
621 shows one main spectral feature of 1100-1400 yrs between 5000 yrs cal BP and the present and two
622 secondary spectral features of 590-1060 yrs between 8000-10000 yrs cal BP and 260-360 yrs cal around
623 6500 yrs cal BP (Figure 3).

624 *Biomarker analysis*

625 Biomarker analyses were performed continuously at a sampling step interval of 1 centimeter all along
626 the sequence. Lipids were extracted from the frozen and dried sediments with dichloromethane and
627 methanol. Alkenones and n-alkanes were isolated using silica gel chromatography and quantified using
628 gas chromatography. The time series derived from these biomarker analyses covers the last 10 000 yrs
629 with a mean temporal resolution of about 15 yrs (Table 1, Jalali et al. 2016).

630 Unsaturation ratio of C37 alkenones was converted into Sea Surface Temperature (SST) using the
631 calibration developed by Conte et al. (2006) (Sicre et al. 2016). The weighted smoothed scalogram
632 displays a significant spectral feature of 2120-2350 yrs from 8000 yrs cal BP to the present. Two
633 significant spectral features of respectively 400-780 and 360-720 yrs are evident between 5500 and 6000
634 yrs cal BP and around 2250 yrs cal BP respectively. Finally, a significant cyclic period of 160-300 yrs
635 is recorded around 4500 yrs cal BP (Figure 3).

636 High-molecular-weight n-alkanes with an odd carbon number, i.e. C₂₇+C₂₉+C₃₁+C₃₃ homologs
637 (TERR-alkanes), were quantified in order to track terrigenous inputs from the Rhône River (Jalali et al.
638 2016). Indeed, these compounds are constituents of epicuticular leaf waxes and their accumulation in
639 the sediments of the Gulf of Lion is primarily associated with vegetation cover changes and soil erosion
640 in the Rhône river catchment. The wavelet spectral analysis presents two major spectral features of
641 1910-2200 yrs between 8000 yrs cal BP and the present and 680-1260 yrs between 6000 and 2000 yrs
642 cal BP. Then, short spectral features of 160-300 and 190-370 yrs are registered around 3000 and 7000
643 yrs cal BP (Figure 3).

644 Finally, the n-alkane Average Chain Length (ACL) was calculated between C₂₇ and C₃₃ in order to
645 derive information on changing moisture conditions and associated vegetation types in the Rhône
646 watershed (Jalali et al. 2017). Under conditions of water deficit, plants actually produce longer chain
647 n-alkane to minimize water loss through evapo-transpiration (Gagosian and Peltzer, 1986). The
648 weighted smoothed scalogram of the ACL time series displays a major significant spectral feature of
649 2520-2700 yrs between 8000 yrs cal BP and the present and another significant spectral feature of
650 750-1260 yrs between 4000 yrs cal BP and the present.

651 The speleothems of “Cueva de Asiul”

652 Smith et al. (2016) recovered two sequences from speleothems labeled ASR and ASM in the Cueva de
653 Asiul, a closed karstic depression in the Cantabrian Cordillera in northwestern Spain (Figure 1). The
654 chronologies of these sequences rely on 10 and 12 U/Th dates respectively. Speleothem ASR grew
655 between 12500 and 500 years BP with a long interruption between 8600 and 4000 years BP. Speleothem
656 ASM grew between 7850 and 0 yrs BP with an interruption between 3800 and 2150 years BP and thus
657 almost entirely spans the gap in the ASR record (Smith et al. 2016 Supplementary information).

658 *Geochemical analysis*

659 Smith et al. (2016) performed calcite δ¹⁸O analysis using an IsoPrime isotope ratio mass spectrometer
660 to track precipitation changes throughout the Holocene. The reliability of the two records within their
661 overlapping period was tested by cross correlation analysis and they were then combined within a single
662 detrended time series (Smith et al. 2016 Supplementary information). The data for this combined and
663 detrended time series were downloaded from the NOAA database for use in our study
664 (<https://www.ncdc.noaa.gov/paleo-search/study/20082>).

665 A monitoring study in Cueva de Asiul demonstrates that the cave’s hydrological system is recharged
666 primarily by winter rainfall and that the isotopic composition of the cave drip waters reflects the δ¹⁸O
667 composition of winter rainfall from the preceding year (Smith et al. 2016 b). Therefore, δ¹⁸O
668 measurements on ASR and ASM speleothems may represent winter rather than annual past precipitation
669 rates over the last 7800 yrs with a mean temporal resolution of 15 yrs (Table 1). The weighted smoothed
670 scalogram of this time series displays a frequency content dominated by a spectral feature of about 1400

671 years between 5000 yrs cal BP and the present. Short spectral features of about 200-450 yrs are also
672 recorded around 500, 1500, 2000 and 4500 yrs cal BP respectively (Figure 3).

673 The Bay of Biscay SST

674 Mary et al. (2017) studied the PP10-07 core recovered in the inner Bay of Biscay, at a point between the
675 Aquitaine shelf and the Cantabrian shelf. The Bay of Biscay is characterized by a complex oceanic
676 circulation. This area is particularly sensitive to North Atlantic subpolar and subtropical gyre dynamics.
677 The chronology of the sequence is based on 10 AMS radiocarbon dates on planktonic foraminifera
678 (Mary et al. 2017). The radiocarbon reservoir age is 405yrs (Reimer et al. 2013). The age model was
679 obtained by a smooth-spline regression (Mary et al. 2017).

680 *SST reconstructions*

681 Mary et al. (2017) derived SSTs from the planktonic foraminifera abundances within the >150µm
682 sediment fraction using the Modern Analogues Technique (Mary et al. 2017). The Annual SST data
683 from the PP10-07 core were retrieved from the Pangea database to be used within our study
684 (<https://doi.pangaea.de/10.1594/PANGAEA.872166>). This time series covers the last 10 000 yrs with a
685 mean temporal resolution of 50 yrs (Table 1). Colder and warmer SST periods are recorded in the Bay
686 of Biscay. They are related to variations in heat transport from the tropics toward Western Europe, due
687 to changes in past dynamics of the Atlantic gyres (Mary et al. 2017).

688 The wavelet analysis of Bay of Biscay SSTs shows a significant spectral feature of 1049-1536 yrs
689 throughout the first half of the Holocene. After 6000 yrs cal BP, a significant spectral feature of 1380-
690 1890 yrs dominates the signal variability. Two short cyclic periods of 140-350 and 240-560 yrs are
691 evidenced around 9000 and 2500 yrs cal BP (Figure 3).

692 Solar activity proxy

693 Two time series for reconstructed solar activity throughout the Holocene are available: Sunspot
694 Number (SN) estimates from a dendro-chronologically dated ¹⁴C record (Solanki et al. 2004) and Total
695 Solar Irradiance (TSI) estimates from several cosmogenic isotope records (Steinhilber et al. 2012).

696 Since these two time series display very similar frequency contents and since the SN time series have
697 a better chronological framework and time resolution, it was decided to use the latter to investigate the
698 presence of solar periodicities in the studied paleoclimate sequences

699 ([ftp://ftp.ncdc.noaa.gov/pub/data/paleo/climate_forcing/solar_variability/](ftp://ftp.ncdc.noaa.gov/pub/data/paleo/climate_forcing/solar_variability/solanki2004-ssn.txt)
700 [solanki2004-ssn.txt](ftp://ftp.ncdc.noaa.gov/pub/data/paleo/climate_forcing/solar_variability/solanki2004-ssn.txt)).

701 ENSO variability

702 During El Niño events, high SSTs off the coast of Ecuador and northern Peru cause positive
703 precipitation anomalies in the western Andean slope. Moy et al. (2002) studied a 9m long core from
704 the Laguna Pallcacocha in the southern Ecuadorian Andes in which light-colored laminae of inorganic
705 and clastic materials related to ENSO-driven episodes of alluvial deposition are recorded. This
706 sequence spans the entire Holocene with a very high temporal resolution allowing to obtain a

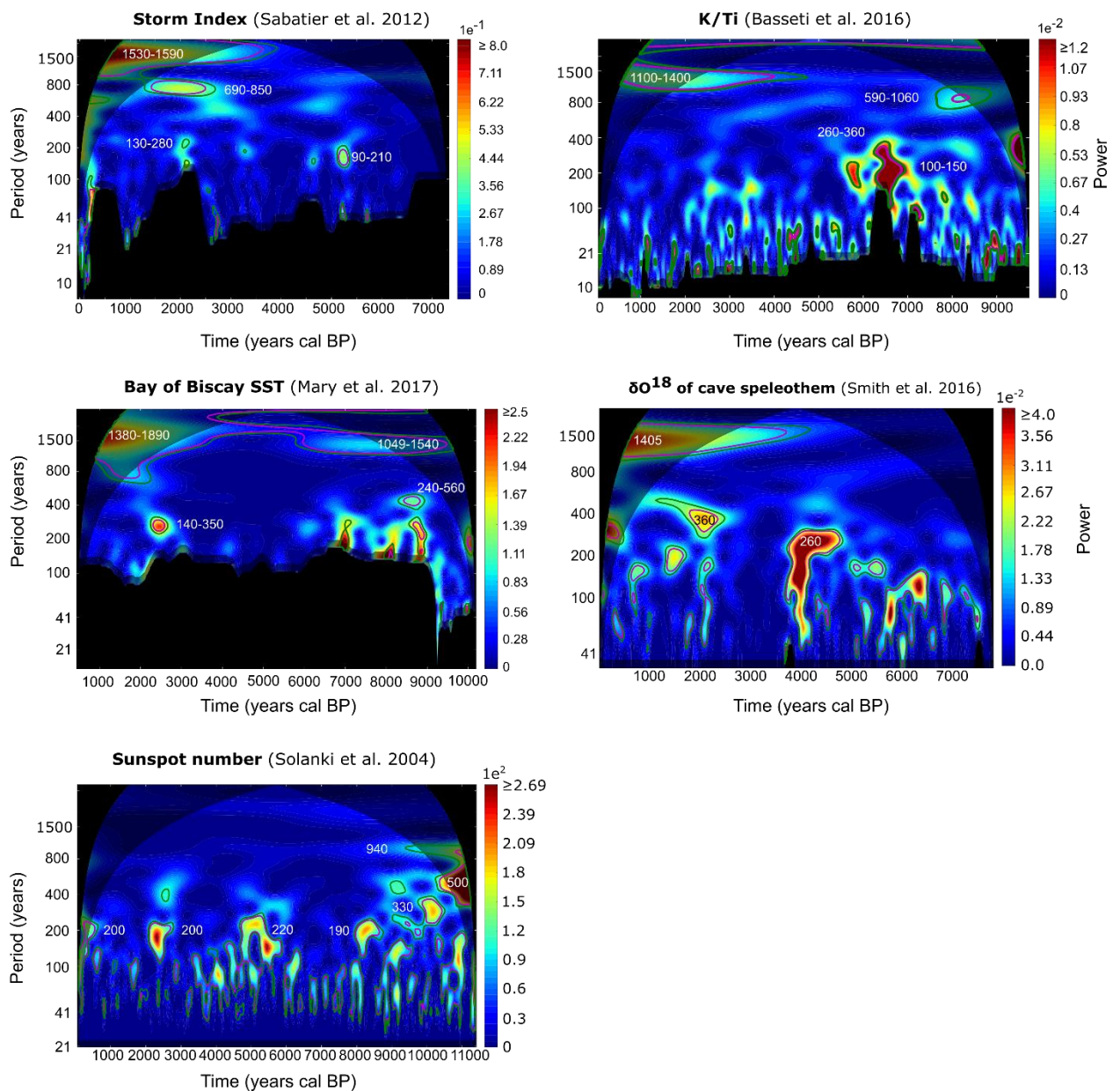
707 continuous record of the pacific climate variability over the last 12000 yrs (NOAA database :
708 [ftp://ftp.ncdc.noaa.gov/pub/data/paleo/paleolimnology/
709 ecuador/pallcacocha_red_intensity.txt](ftp://ftp.ncdc.noaa.gov/pub/data/paleo/paleolimnology/ecuador/pallcacocha_red_intensity.txt)). The age model was obtained by combining the correlation of
710 laminae with radiocarbon dated laminae in a neighboring core and an “event model” assuming that
711 each single high terrigenous deposition events within the core correspond to a single ENSO event.
712 Because of the complexity of the method used to obtain this age model, it was not possible for us to
713 propagate age model uncertainties within wavelet spectral analysis of this time series.

714 *Red color intensity*

715 The concentration of light-colored clastic laminae along the sequence was estimated by scanning the
716 core with Geotek line scan camera, which generates a continuous red, green and blue digital record of
717 the sediment surface. The red color channel was selected to document ENSO variability because it
718 displays an higher variance than either blue and green channels.

719

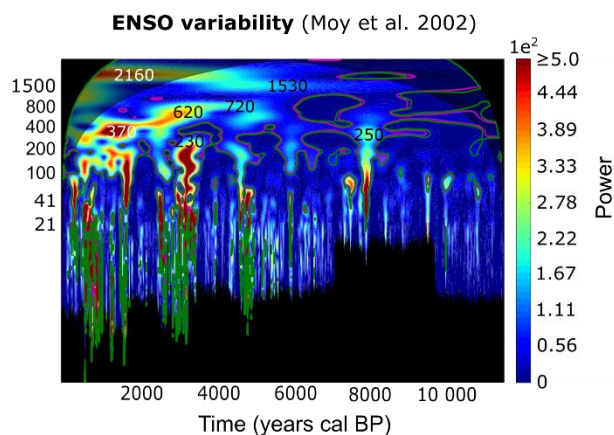
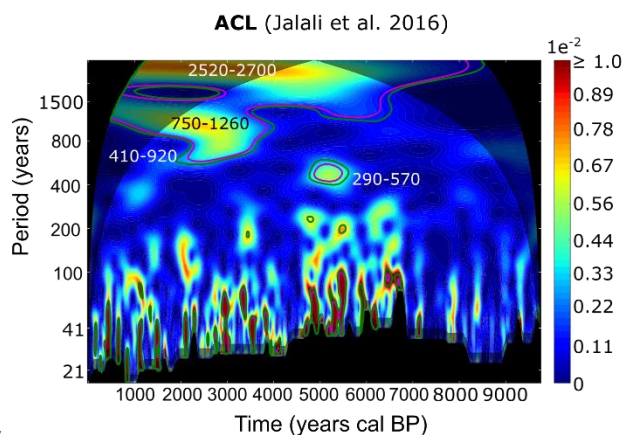
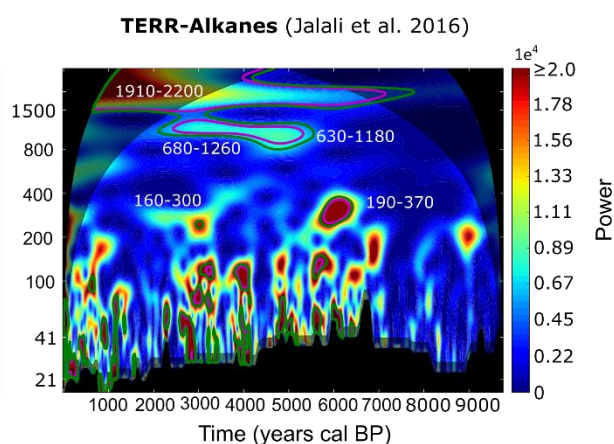
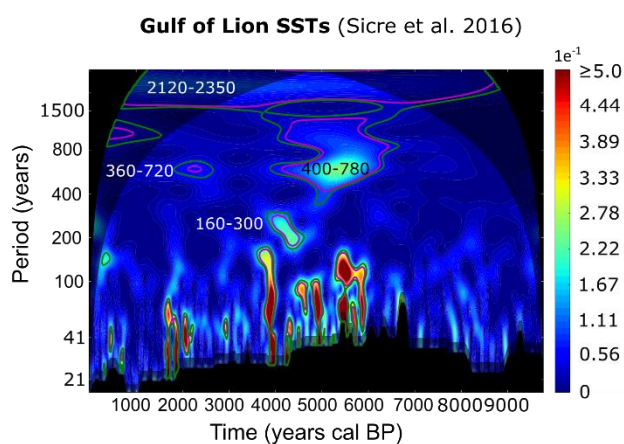
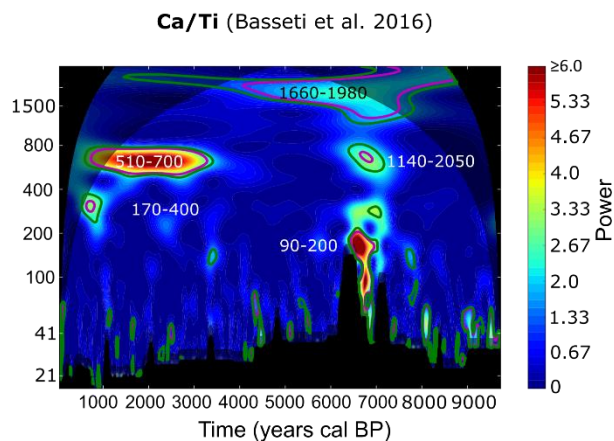
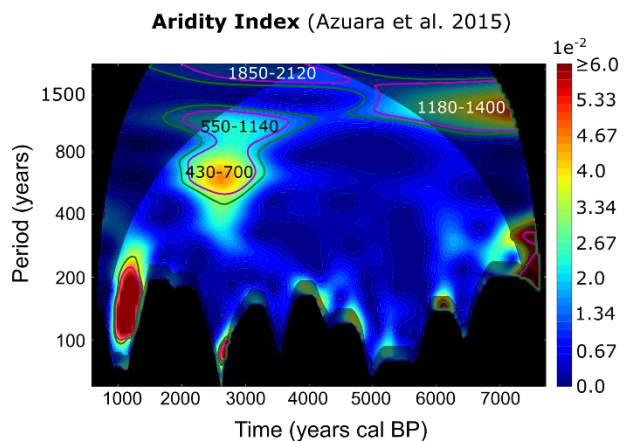
720



721

722

723 *Figure 3 (part 1): Weighted smoothed scalograms of the studied time series. Colors indicate the*
 724 *amplitude of the wavelet power spectra, red being the highest amplitudes and blue the lowest. The*
 725 *purple lines represent the 95% confidence level, the green lines the 90% confidence level. The lateral*
 726 *grey shaded area represents the cone of influence and the lateral black areas the part of the time-scale*
 727 *plane excluded from the analysis because of the fixed length of integration for the smoothing of the*
 728 *scalogram. The black and the grey shaded area at the bottom of each scalogram represent the SNEZ*
 729 *and its extension. Characteristic periods of main spectral features taking into account age model*
 730 *errors are reported in black or white. Since the time series differ in length and resolution, scales are*
 731 *different from one spectrum to another.*



732

733 *Figure 3 (part 2): see legend for Figure 3 (part 1).*

734

735

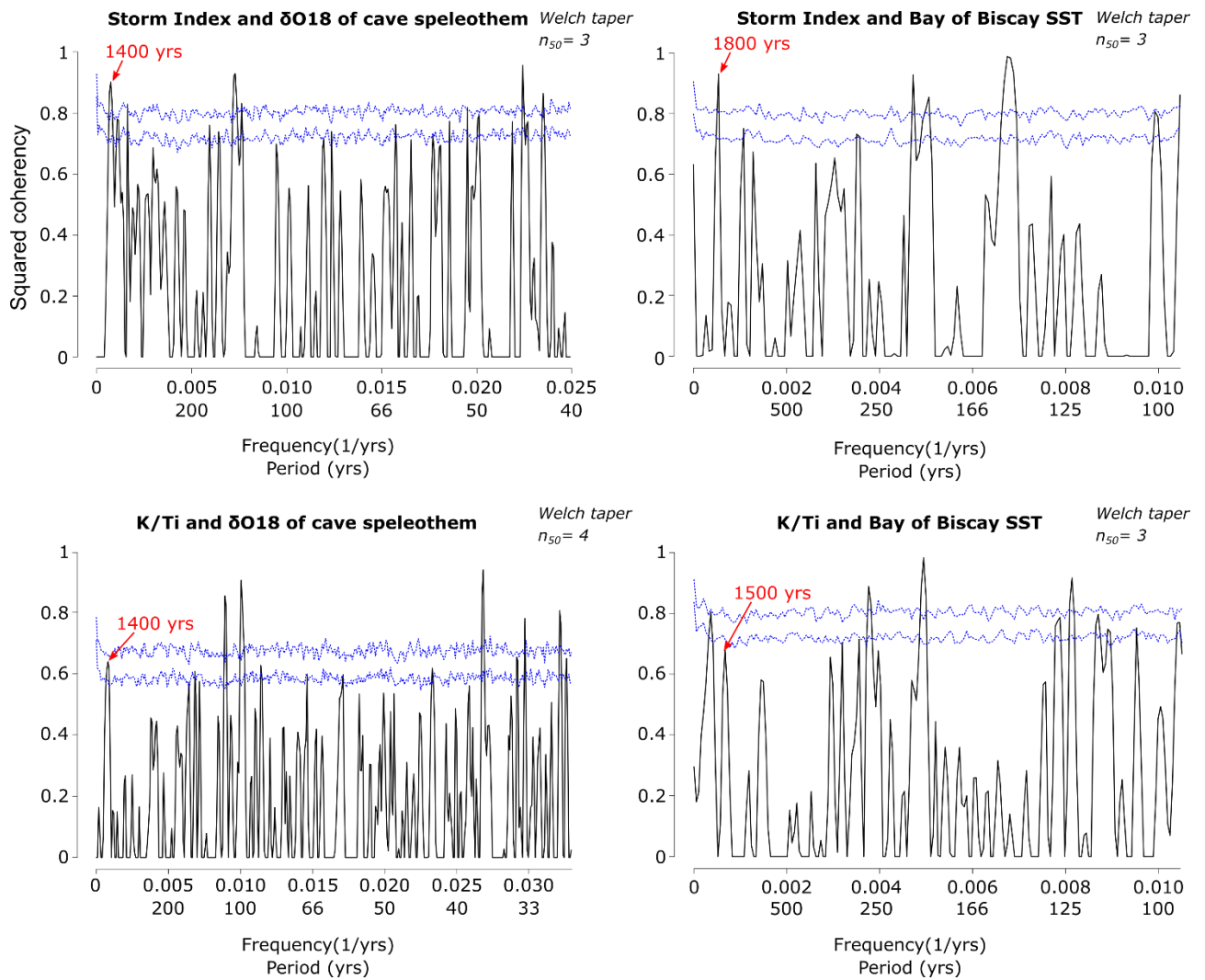
736 **Discussion**

737 In this section, the frequency contents of each different paleoclimate proxy are compared to one another
738 in order to better understand Holocene climate variability and its underlying mechanisms.

739 Oceanic forcing? The 1500 yrs cyclic period

740 SI, and K/Ti ratio time series from the Gulf of Lion on one hand and speleothem $\delta^{18}\text{O}$ and Bay of Biscay
741 SST time series from the near Atlantic area on the other hand, display similar significant spectral features
742 after 5000 yrs cal BP characterized by periods of respectively 1530-1590, 1100-1400, 1405 and 1380-
743 1890 yrs (Figure 3). This low frequency periodicities are also significantly recorded using REDFIT
744 program (Appendix 1). The coherency spectra of Gulf of Lion time series with Atlantic ones confirm
745 that they are indeed significant shared spectral features, except in the case of the K/Ti ratio and the Bay
746 of Biscay SST in which a marked but non-significant spectral peak at 1500 yrs is detected (Figure 4).
747 These results highlight a link between the climate of the Atlantic area and the Gulf of Lion. The
748 comparison of these sequences filtered with a 1450-1550 yrs passband filter highlights time intervals of
749 high (or low) storm activity in the Gulf of Lion that correspond to lower (or higher) precipitation in
750 northwestern Spain and cooler (or warmer) SSTs in the Bay of Biscay since 5000 yrs cal BP (Figure 5).
751 The oscillations also visible in the K/Ti ratio are more difficult to interpret. Insofar, as this proxy is an
752 indicator of the sediments source, these fluctuations must be linked to changes in precipitation regime
753 within the Rhone watershed causing changes of eroded areas. The time series are slightly off-set from
754 each other, but these discrepancies are consistent with the order of magnitude of the age models'
755 uncertainties (Table 1).

756

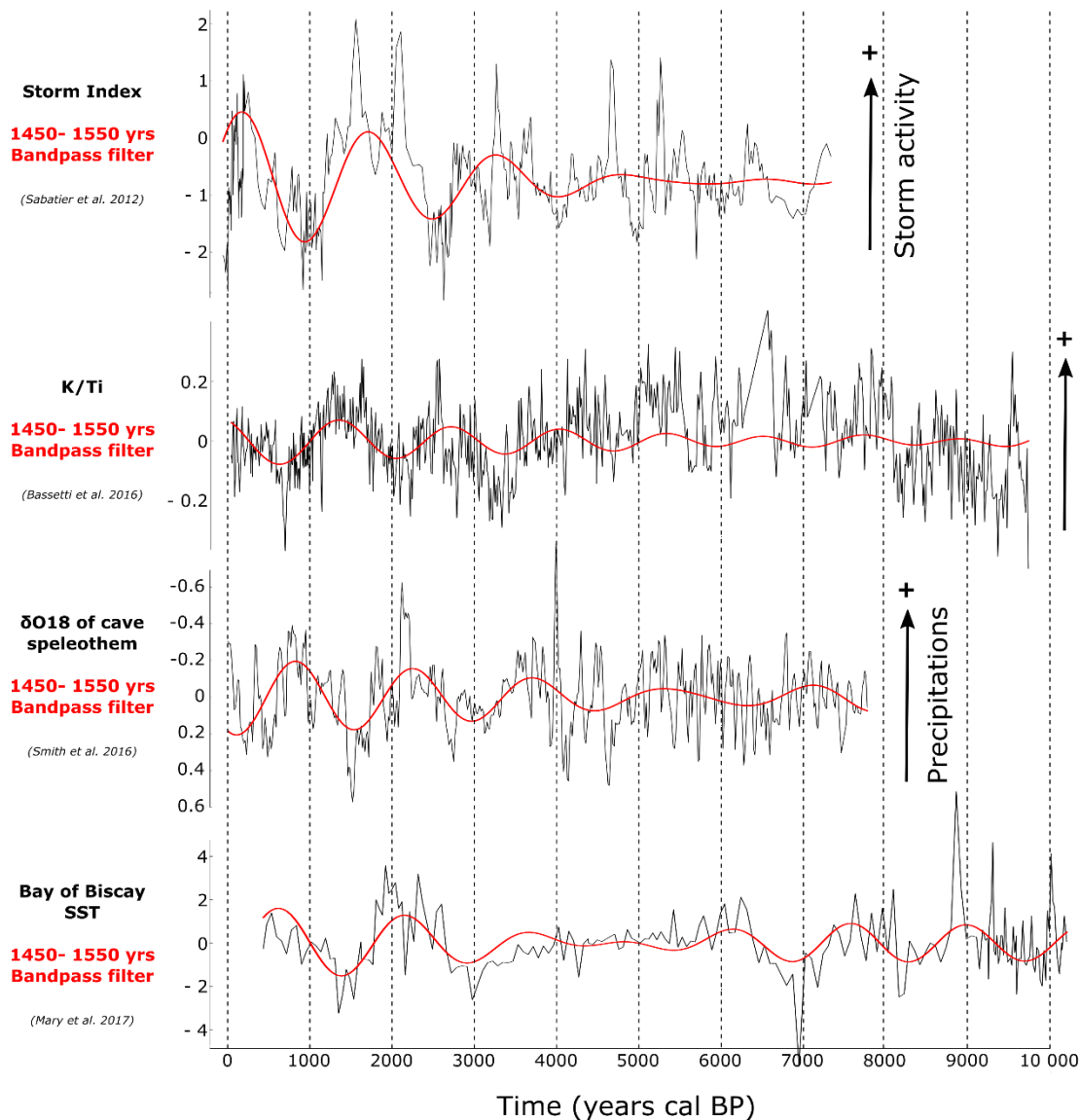


757

758 *Figure 4: Coherency spectrum of the Palavas Storm Index and K/Ti ratio time series with the Atlantic*

759 *paleoclimatic proxies, Cave speleothem $\delta^{18}O$ and Bay of Biscay SST. The dashed blue lines represent*

760 *the 0.90 and 0.95 confidence levels and the spectral peaks of interest are pointed with a red arrow.*

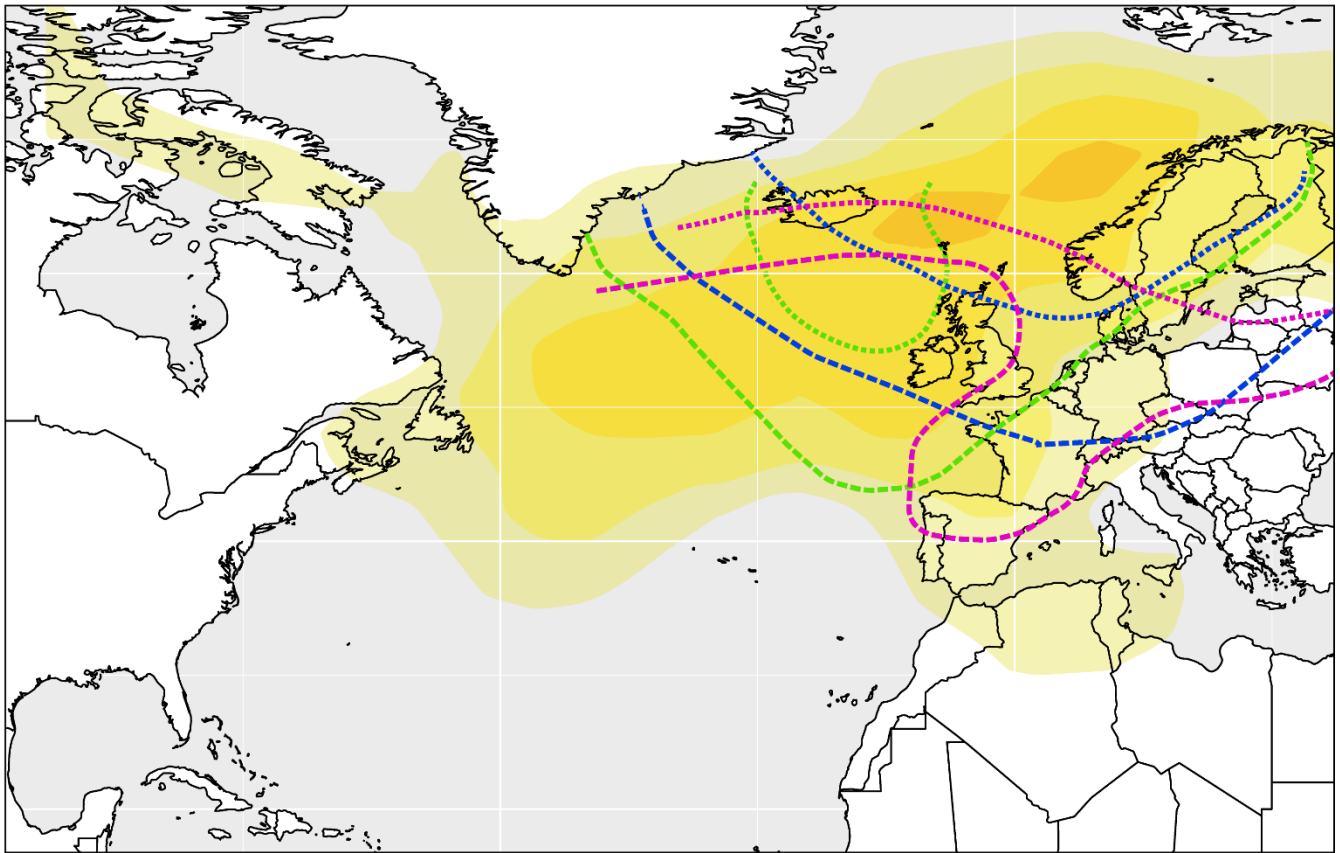


761
 762 *Figure 5: Comparison of the Palavas Storm Index (SI), the K/Ti ratio from the Gulf of Lion, the Asiul*
 763 *Cave speleothem $\delta^{18}O$, and the Bay of Biscay SSTs filtered with a 1450-1550 yrs bandpass filter to*
 764 *highlight variations linked to the ~1500 yrs cycles. The Bay of Biscay SSTs record from the PP 10-07*
 765 *core (dashed blue curve, Mary et al. 2017) studied in this article is completed here with the SSTs record*
 766 *from the MD03-2693 core (dashed green curve, Mary et al. 2015) to show the important decrease in*
 767 *Bay of Biscay SSTs at the last part of the sequence.*

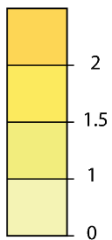
768 Such ~1500 oscillations were first characterized by Bond et al. (2001) within stacked Ice Rafted Debris
 769 (IRD) records from the north Atlantic. Nevertheless, their gradual appearance during the second part of
 770 the Holocene and thus their non-stationarity, was first described by Debret et al. (2007) in several North
 771 Atlantic climate proxies including Bond's stacked IRD time series. Based on the predominance of this
 772 pattern in proxies specifically recording water mass activity in the Atlantic, Debret et al. (2007, 2009)
 773 assumed that this variability reflected changes in the Atlantic thermohaline circulation. The detection of
 774 a similar cyclic period in the Bay of Biscay SSTs, which depend on the dynamics of Atlantic gyres,

775 supports this hypothesis and further implies that these changes affect both deep and surface Atlantic
776 waters. On the other hand, this ~1500 yrs variability is also evidenced in proxies related to mid-latitude
777 atmospheric circulation. Indeed, such cycles are also recorded in a storminess record from north-western
778 Europe (Sorrel et al 2012) in phase with the high storm activity periods registered in the Gulf of Lion
779 (Sabatier et al. 2012). Moreover, the speleothem $\delta^{18}\text{O}$ from northwestern Spain, which also displays
780 these cycles, is related to advection of Atlantic low-pressure systems over the Iberian Peninsula. Thus,
781 if internal fluctuations of the Atlantic thermohaline circulation are actually responsible for these late
782 Holocene ~1500 years cyclic period, what mechanism might explain the fact that this frequency pattern
783 also affects past atmosphere dynamics?

784 Experiments using ocean/atmosphere coupled models show an influence of the Atlantic Meridional
785 Overturning Circulation (AMOC) on Atlantic storm track strength and position during winter time
786 (Brayshaw et al. 2009, Woolings et al. 2012, Harvey et al. 2015). The Atlantic storm track is an area
787 where depressions form preferentially and travel down the prevailing winds. Its strength corresponds to
788 the number and the importance of the lows formed during a given period and is quantified using the
789 variance of the Mean Sea Level Pressure (MSLP). In models, AMOC weakening causes a strengthening
790 of the storm track which spreads eastwards over northern Europe (Figure 6). The weaker heat transport
791 from the tropics toward the pole, because of the AMOC slowdown, induces cooler SSTs in the North
792 Atlantic and increases sea ice extent in the Arctic. The resulting increase in the mid-latitude temperature
793 gradient causes an increase in baroclinicity and thus cyclogenesis (Raible et al. 2007, Brayshaw et al.
794 2009, Woolings et al. 2012, Harvey et al. 2015). This mechanism would explain why a periodic
795 weakening of the AMOC induces lower SSTs in the Bay of Biscay and causes an increase in storminess
796 in northwestern Europe (Sorrel et al. 2012) by a direct increase in the number of depressions advected
797 over this area.



Regression slopes quantifying the storm track response to AMOC reduction (1/10 hPa).



500 hPa height for large scale circulation patterns causing meridional flows from the mediterranean toward the north, over southern France



Western low



Cyclonic northwesterly



Cyclonic southwesterly

(Woolings et al. 2012)

(Nuissier et al. 2011)

799 Figure 6: Comparison of the storm track response to AMOC reduction in experimental models
 800 (Woolings et al. 2012) and position of the lows during large scale circulation patterns which cause
 801 Mediterranean air masses to flow northwards over southern France, thereby perhaps leading to higher
 802 storm frequencies in the Gulf of Lion (Nuissier et al. 2011).

803 In the Gulf of Lion, heavy precipitation events and marine storms are both linked to the northward flow
 804 of warm, moist air masses from the Mediterranean, bringing humidity over areas of high relief and
 805 associated with very strong south-easterly to south-westerly winds ($>40 \text{ m.s}^{-1}$) in the case of marine
 806 storms (Sabatier et al. 2008). Nuissier et al. (2011) identified the different Large-Scale Circulation
 807 patterns (LSC) leading to such northward flows of Mediterranean air masses by analyzing

808 meteorological data for wintertime between 1960 and 2000. The 500 hPa heights describing the altitude
809 pressure field of these LSCs are reported on the map showing the response of the Atlantic storm track
810 to AMOC weakening (Figure 6). The area of enhanced storm track strength encompasses the location
811 of the low-pressure systems which could induce heavy precipitations and storms in the Gulf of Lion.
812 Therefore, repetitive weakening of the AMOC, which strengthens the Atlantic storm track, could also
813 explain the ~1500 yrs spectral feature evident in the Palavas SI. Regarding the fluctuations in the K/Ti
814 ratio, it is possible that the periods of greater storm frequency also have caused a greater sediments
815 contribution from the southern part of the Rhone watershed due to more frequent heavy precipitation
816 events. However, further studies are necessary to test this hypothesis.

817 Finally, Brayshaw et al. (2009) highlight the fact that a weakening of the AMOC can cause a decrease
818 in winter precipitation over all of Western Europe, including the western Mediterranean area. Indeed,
819 the SST reduction over the North Atlantic reduces the saturation water vapor pressure. Thus, despite the
820 stronger zonal flow, the air masses from the Atlantic advected over Western Europe are cooler and drier.
821 Since the speleothem $\delta^{18}\text{O}$ from northwestern Spain probably records winter precipitation in a region
822 that is very sensitive to Atlantic influences (Smith et al. 2016), it makes sense that high storm activity
823 periods are associated with lower precipitation in the northern Iberian Peninsula. Especially since more
824 frequent storms and heavy precipitation events in the Gulf of Lion are linked to the advection of
825 moisture-laden northward air masses originating from the Mediterranean and not eastward air masses
826 from the Atlantic (Nuissier et al. 2011).

827 All of this evidence is consistent with several weakening of the AMOC during the latter part of the
828 Holocene. Such variations are consistent with the well-known Bond events evident in North Atlantic
829 IRD records (Bond et al. 2001). Sgubin et al. (2017) highlight that an important proportion (45.5%) of
830 global climate models, which reproduce more accurately the structure of the North Atlantic Ocean, are
831 predicting an imminent local collapse of the deep ocean convection in the Labrador Sea linked to the
832 ongoing climate change. This possible interruption of deep-water formation could be similar to periodic
833 weakening of the AMOC. Therefore, understanding the cause and the mechanism of such millennial
834 scale climate variability appears crucial to improve our ability to predict the future climate.

835 Solar forcing: 210 yrs cyclic periods

836 The two short spectral features of about ~200 yrs displayed in the SI time series around 2500 and 5500
837 yrs cal BP (Figure 3) look similar in term of period and time interval to the 210 yrs so called De Vries
838 cycles evidenced in solar activity proxies (Figure 6) (Stuiver and Braziunas 1989, Debret et al. 2007,
839 Ma 2007, Debret et al. 2009, Steinhilber et al. 2012, Usokin et al. 2016). The possibility of shared
840 spectral features between Gulf of Lion storminess records and solar variability proxies is further
841 supported by a ~270 yrs periodicity found within a storminess record spanning the last 3000 yrs from
842 the Bagnas pond, located about 40 km from Palavas, (Degeai et al. 2016). However, we were not able
843 to detect any significant shared spectral features corresponding to De Vries cycles in the SI time series

844 using coherency analyses. This is not surprising since the De Vries cycles are highly non-stationary
845 and the WOSA algorithm on which the REDFITX consistency analyses are based assumes a stationary
846 signal. Nevertheless, it makes it difficult to draw any conclusions. Several studies conducted in Europe
847 and in the Mediterranean also provide evidence for increases in precipitation and flood frequencies
848 related to centennial scale solar variability (Wirth et al. 2013, Czymzik et al. 2016, Sabatier et al.
849 2017, Zielhofer et al. 2017). Results suggest that centennial scale changes in solar irradiance strongly
850 affect atmospheric circulation in the European Atlantic sector inducing NAO-like variability (Raible et
851 al. 2007, Martin-Puertas et al. 2012). However, for now, no reliable reconstructions of the past NAO
852 variability covering the entire Mid and Late Holocene period is available (Ortega et al. 2015, Franke et
853 al. 2017). Thus, further work is needed to better address this issue.

854 ENSO influences?

855 The major changes in SST and atmospheric surface pressures characterizing the ENSO variability in the
856 tropical Pacific, also affect climate variability at higher latitudes in very remote parts of the globe
857 (Brönnimann et al. 2007). Many studies relying on instrumental data (Loon and Madden, 1981;
858 Fraedrich 1990, 1994; Fraedrich and Müller, 1992; May and Bengtsson, 1998; Mariotti et al. 2002;
859 Xoplaki 2002 ; Gouirand and Moron, 2003; Moron and Gouirand, 2003; Muñoz-Diaz and Rodrigo,
860 2005; Mariotti et al. 2005; Pozo-Vazquez et al. 2005) and on experiments based on Ocean-atmosphere
861 coupled models (Raible et al. 2001, 2004; Deser et al. 2006; Brönnimann et al. 2007) support a non-
862 stationary but significant influence of ENSO variability on Western Europe including the Western
863 Mediterranean. Such remote influence of the pacific area on the European climate is further supported
864 by results from climate reconstructions over the last centuries (Mann et al. 2000, Rimbu et al. 2003,
865 Brönnimann et al. 2007, Balting et al. 2020). Therefore, in this section our attention focuses on the
866 potential influence of ENSO variability on the northwestern Mediterranean climate throughout the mid-
867 to late Holocene.

868 To address this issue, the frequency content of western Mediterranean paleoclimate sequences was
869 compared with the frequency content of a high-resolution ENSO variability record from the Ecuadorian
870 Andes spanning the Holocene (Moy et al. 2002) (Figure 3).

871 The ENSO variability record shows some interesting spectral features which might correspond to
872 unattributed ones in our Mediterranean sequences (Figure 3). In the ENSO time series, the significant
873 spectral feature with a period of 620 yrs between 2000 and 4000 yrs cal BP, gradually changing to a
874 period of 720 yrs between 4000 and 6000 yrs cal BP (Figure 3) remind the following significant spectral
875 features in Mediterranean sequences:

- 876 i. 430-700 yrs between 2000 and 3000 yrs cal BP (AI)
- 877 ii. 510-700 yrs between 1000 and 3000 yrs cal BP (Ca/Ti)
- 878 iii. 360-720 yrs around 2000 yrs cal BP and 400-780 yrs between 4000 and 6000 yrs cal BP (Gulf

879 of Lion SST)

880 iv. 630-1260 yrs between 2000 and 5000 yrs cal BP (TERR-Alkanes)

881 These similarities are confirmed by the coherency analyses with the ENSO variability time series
882 which all display a significant spectral peak around 600 yrs for AI, Ca/Ti and Gulf of Lion SST and
883 around 750 yrs for TERR-Alkanes (Figure 7).

884 In a similar way, the ENSO ~2160 yrs significant spectral feature between the present and 6000 yrs cal
885 BP (Figure 3) remind the following significant spectral features in the Mediterranean sequences:

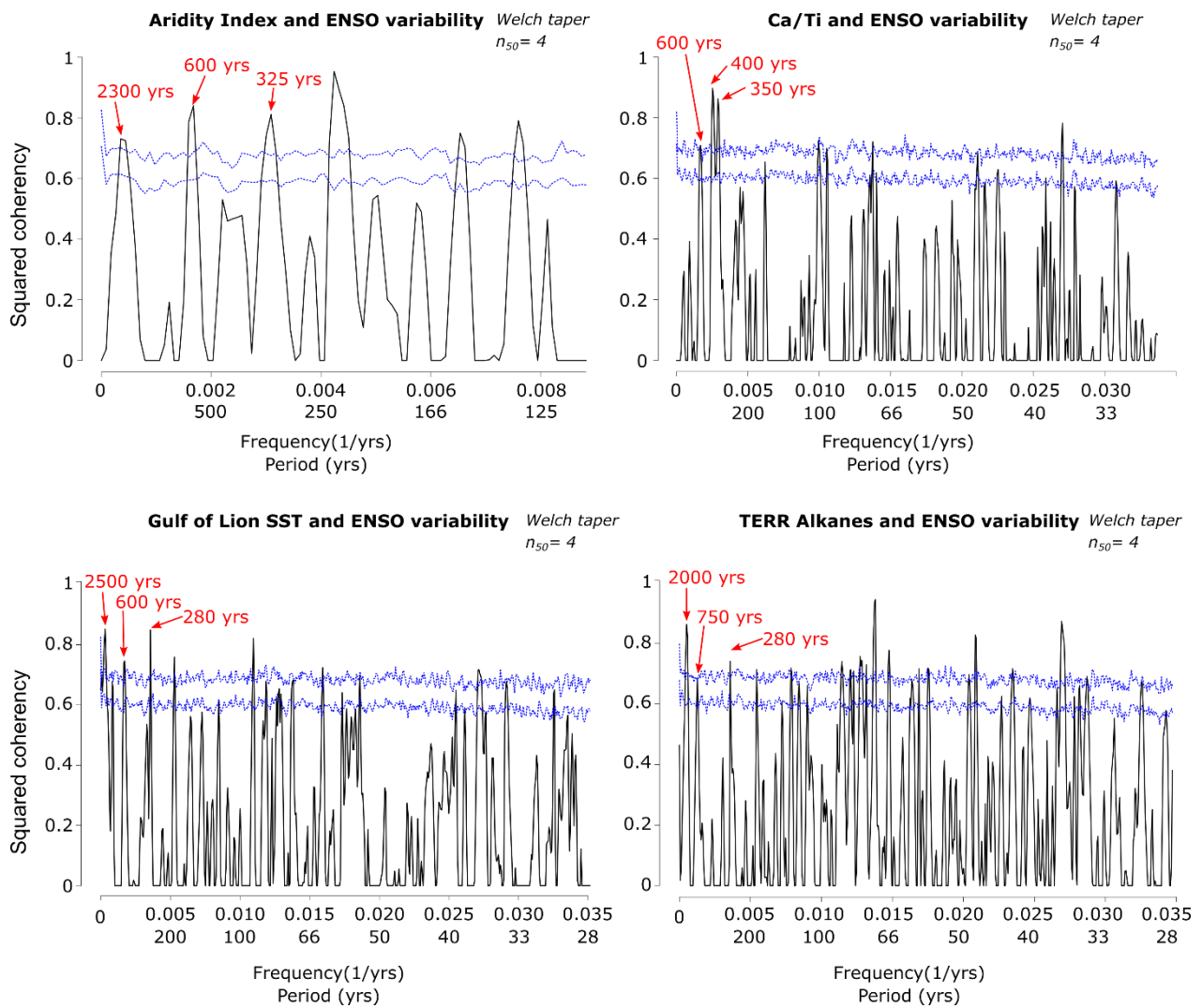
886 i. 1850-2120 yrs between 1000 and 5000 yrs cal BP (AI)

887 ii. 2120 -2350 yrs between the present and 6000 yrs cal BP (Gulf of Lion SST)

888 iii. 1910-2190 yrs between the present and 7000 yrs cal BP (TERR-Alkanes)

889 Again, these similarities are confirmed by coherency analyses with the ENSO time series which
890 display significant peaks around 2300 (AI), 2500 (Gulf of Lion SST) and 2000 yrs (TERR-Alkanes)
891 (Figure 7).

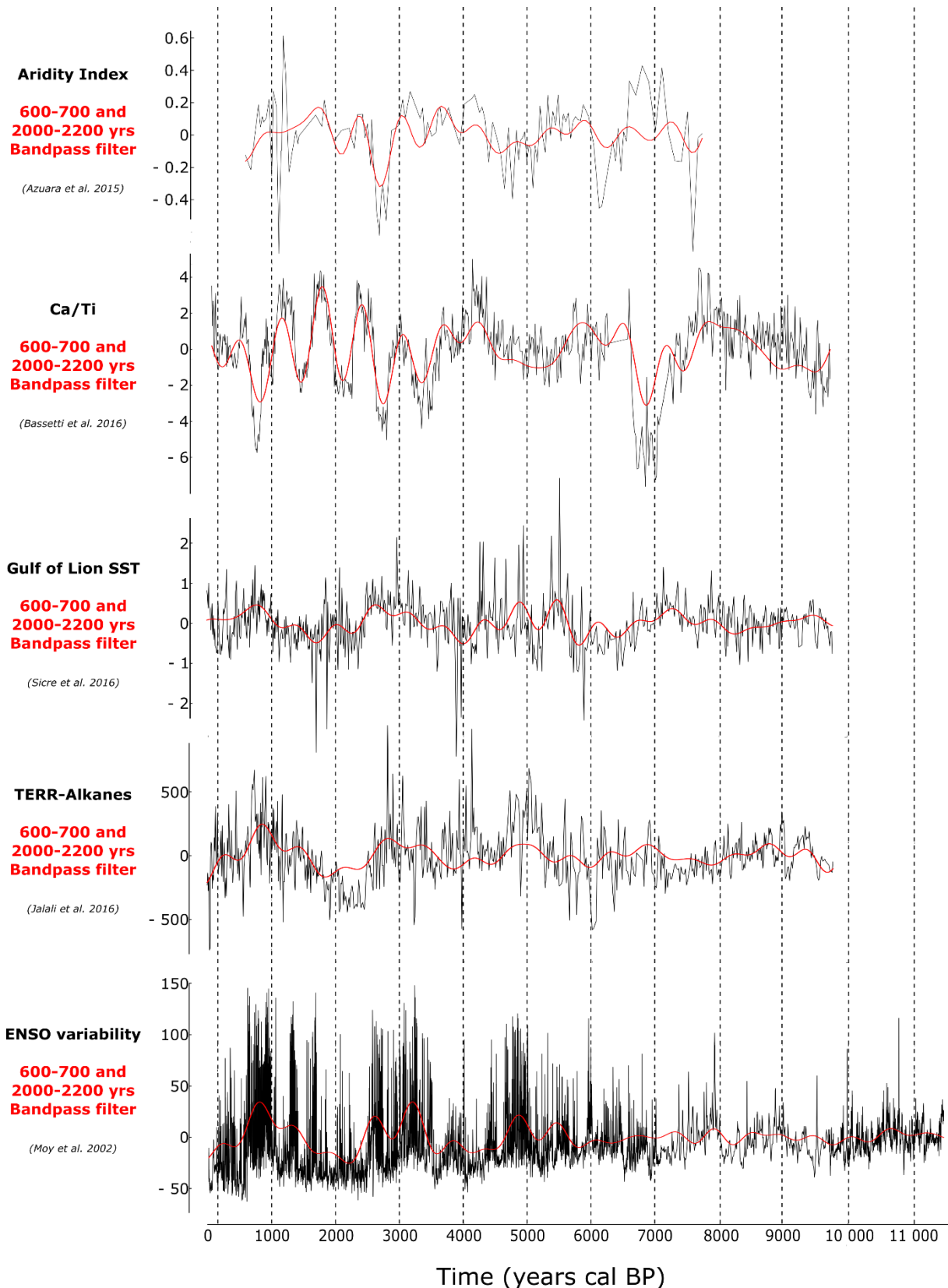
892 Finally, coherency analyses between the ENSO variability and AI and Ca/Ti time series allow to
893 highlight significant peaks around 350 and 325 yrs while coherency analyses with Gulf of Lion SST
894 and TERR-Alkanes time series display significant peaks around 280 yrs (Figure 7). However, the
895 comparison of the scalograms of these times series show that these significant peaks may be spurious
896 shared features related to the violation of the hypothesis of stationarity since all these signals displays
897 more or less marked spectral features around periods of 300 yrs in wavelet spectral analyses, however
898 they never occurred at the same time as in the ENSO signal.



899

900 Figure 7: *Coherency spectrum of the Palavas Aridity Index, the Ca/Ti ratio, the Gulf of Lion SST and*
 901 *the TERR-Alkanes time series with the ENSO variability proxy. The dashed blue lines represent the 0.90*
 902 *and 0.95 confidence levels and the spectral peaks of interest are pointed with a red arrow.*

903 The comparison of these sequences filtered with 600-700 and 2000-2200 yrs passband filters clearly
 904 show that these shared spectral features play a major role in the millennial and centennial scale
 905 variability of these time series (Figure 8). Moreover, these results highlight the remarkable similarities
 906 of the ENSO variability time series with the TERR-Alkanes and the Gulf of Lion SST. Periods of higher
 907 ENSO variability clearly correspond to periods of enhanced erosion and thus probably enhanced rainfall
 908 in southern France, as well as periods of higher SST in the Gulf of Lion (Figure 8). On the other hand,
 909 the AI and Ca/Ti time series do not show any obvious similarities with ENSO variability apart from the
 910 spectral signatures already discussed. It is very interesting to note that these shared periodicities arise
 911 during the second part of the Holocene after 5000 yrs cal BP simultaneously with a regime shift toward
 912 a dynamics characterized by more frequent and stronger EL Niño events (Tsonis 2009).



913

914 *Figure 8: Comparison of the Aridity Index (SI), the Ca/Ti ratio, the Gulf of Lion SST, the TERR-Alkane*
 915 *and the ENSO variability time series filtered with 600-700 and 2000-2000 yrs bandpass filter to*
 916 *highlight variations linked to the shared spectral features detected in these sequences.*

917

918 One of the mechanisms explaining such a remote connection between the past climate variability in the
919 Pacific area and the western Mediterranean that has been most studied, involves a downstream
920 propagation of ENSO impact along a North-Pacific/North-Atlantic connection during boreal winters.
921 The season-averaged mid-latitude atmospheric circulation can be broken down into two components: (i)
922 the zonal mean flow and (ii) asymmetric features arising from irregularities of the earth's surface
923 (mountains, continent-ocean contrast, sea surface temperature asymmetries, etc.) referred to as
924 stationary waves (Held et al. 2002, Nigam and DeWeaver, 2003). During boreal winters, when the
925 amplitude of these stationary waves is maximal in the Northern Hemisphere (Nigam and DeWeaver,
926 2003), the ENSO events may change their structure by disrupting Hadley's circulation (Brönnimann et
927 al. 2007). Such a change of the quasi-stationary wave over the north Atlantic can impact, among other
928 things, on the cyclogenesis of this area, the Icelandic low, the Azores high and the NAO variability (e.g.
929 Cassou and Terray, 2001, Honda et al. 2001, Raible 2001, Moron and Gouirand 2003). ENSO could
930 also affect European climate through a downward propagation of stratospheric anomalies (e.g. Randel,
931 2004; Manzini et al. 2006).

932 Further research is needed to better understand the relative importance of the different Pacific/Atlantic
933 coupling mechanisms, and the link between ENSO and European climate at the decadal and
934 multidecadal scale (Brönnimann et al. 2007). However, our results and the studies mentioned above
935 make the ENSO influence a credible hypothesis to explain the similarities between records in the north-
936 western Mediterranean and those in the eastern Pacific. On the other hand, the shared spectral features
937 between the tropical Pacific and the western Mediterranean time series could also arise from an
938 independent climate forcing, which might influence both ENSO and the Mediterranean variability
939 without implying any direct link between them. This could be particularly the case for the significant
940 spectral feature of period ~2200 yrs recorded during the second half of the Holocene in the ENSO, AI
941 Gulf of Lion SST and TERR-alkanes time series. Indeed, it reminds 2100-2400 yrs periodicity (Hallstatt
942 cycles) discussed in solar activity proxies but that we haven't been able to detect significantly neither
943 with wavelet spectral analysis nor with the WOSA algorithm (Figure 3 and Appendix 1) (Stuiver and
944 Braziunas 1989, Debret et al. 2007, Ma 2007, Debret et al. 2009, Steinhilber et al. 2012, Usokin et al.
945 2016). Thus, further investigation is needed to accurately address the question of the potential influence
946 of ENSO variability on the north-western Mediterranean climate throughout the Holocene. However, a
947 review of the frequency content of a full set of paleoclimatic time series from the tropical areas in order
948 to investigate this issue is a huge task beyond the scope of this article.

949 **Conclusion**

950 Seven paleoclimate time series from the Gulf of Lion, together with time series recording the Atlantic
951 climate and ENSO past variability, were compared in the frequency domain using wavelet analysis for
952 irregularly sampled signals. Since direct comparison of all of their oscillations is not informative, the
953 comparison of their frequency content is used to discuss directly the forcing and mechanism underlying

954 Mediterranean climate variability. Indeed, two groups of shared spectral features may be defined on the
955 basis of the results of our analysis: (i) an Atlantic spectral feature of ~1500 yrs since 5000 yrs cal BP,
956 and (ii) tropical Pacific spectral features of 600-700 and ~2100 yrs recorded respectively around 2500,
957 and during the second part of the Holocene. The Atlantic cyclic period of ~1500 yrs is probably related
958 to repetitive fluctuations of the Atlantic thermohaline circulation which induces changes in the storm
959 track extension and position, with impacts on both precipitation and storminess in the Gulf of Lion over
960 millennial scale. On the other hand, the tropical Pacific features recorded in many climate proxies from
961 the Gulf of Lion, might highlight the influence of the ENSO climate variability over the western
962 Mediterranean.

963 Of course, further studies are needed to fully characterize and understand Mediterranean climate
964 variability during the Holocene period. However, it is interesting to note that the Atlantic paleoclimatic
965 variability, which is often considered as one of the main factors influencing past Western Mediterranean
966 climate, is clearly detected in only two of the seven proxies analyzed while possible tropical features are
967 clearly highlighted. The link between the tropical latitudes and the Mediterranean Basin needs to be
968 better characterized. One might also wonder to what extent the leading mechanisms of climatic change
969 described here influence and control climatic variability in the Eastern Mediterranean, considering the
970 east-west see-saw pattern described by Roberts et al. (2012). We might also ask whether the described
971 patterns are valid in the southern Mediterranean realm, given the north-south paleohydrological contrast
972 reported by Magny et al. (2013). Nevertheless, the results presented in this review article establish a
973 state of the art for paleoclimate variability in the north-western Mediterranean area. Wavelet spectral
974 analyses allows us to understand the “natural” millennial and centennial scale variability of the earth’s
975 climate system in this climatic change hot spot (Giorgi, 2006).

976 **Acknowledgements**

977 This research was funded by MISTRALS/PALEOMEX meta-program, the CNRS and the French
978 Museum of National History (MNHN). Paleoclimate time series were extracted from the PANGEA and
979 the NOAA database and the work of the data contributors and the PANGEA and NOAA communities
980 is gratefully acknowledged. None of the authors have conflicts of interest to declare. The crew operating
981 the GMO2-Carnac (R/V *Le Suroît* retrieving core KSGC31) and GolHo (R/V *Néréïs*) cruises are
982 thanked.

983 **References**

- 984 Alley, R.B., Mayewski, P.A., Sowers, T., Stuiver, M., Taylor, K.C., Clark, P.U., 1997.
985 Holocene climatic instability: A prominent, widespread event 8200 yr ago. *Geology* 25,
986 483–486.
- 987 Anchukaitis, K.J., Tierney, J.E., 2013. Identifying coherent spatiotemporal modes in time-
988 uncertain proxy paleoclimate records. *Climate Dynamics* 41, 1291–1306.
989 <https://doi.org/10.1007/s00382-012-1483-0>

- 990 Azuara, J., Combourieu-Nebout, N., Lebreton, V., Mazier, F., Müller, S.D., Dezileau, L., 2015.
 991 Late Holocene vegetation changes in relation with climate fluctuations and human activity
 992 in Languedoc (southern France). *Climate of the Past* 11, 1769–1784.
 993 <https://doi.org/10.5194/cp-11-1769-2015>
- 994 Azuara, J., Lebreton, V., Peyron, O., Mazier, F., Combourieu-Nebout, N., 2018. The Holocene
 995 history of low altitude Mediterranean *Fagus sylvatica* forests in southern France. *Journal of*
 996 *Vegetation Science* 29, 438–449.
- 997 Balting, D.F., Ionita, M., Wegmann, M., Helle, G., Schleser, G.H., Rimbu, N., Freund, M.B.,
 998 Heinrich, I., Caldarescu, D., Lohmann, G., 2020. Large scale climate signals of a European
 999 oxygen isotope network from tree-rings – predominantly caused by ENSO
 1000 teleconnections? *Climate of the Past Discussions* 1–24. <https://doi.org/10.5194/cp-2020-39>
- 1001 Bar-Matthews, M., Ayalon, A., 2011. Mid-Holocene climate variations revealed by high-
 1002 resolution speleothem records from Soreq Cave, Israel and their correlation with cultural
 1003 changes. *The Holocene* 21, 163–171. <https://doi.org/10.1177/0959683610384165>
- 1004 Bassetti, M.-A., Berné, S., Sicre, M.-A., Dennielou, B., Alonso, Y., Buscail, R., Jalali, B.,
 1005 Hebert, B., Menniti, C., 2016. Holocene hydrological changes in the Rhône River (NW
 1006 Mediterranean) as recorded in the marine mud belt. *Climate of the Past* 12, 1539–1553.
 1007 <https://doi.org/10.5194/cp-12-1539-2016>
- 1008 Billeaud, I., Tessier, B., Lesueur, P., 2009. Impacts of late Holocene rapid climate changes as
 1009 recorded in a macrotidal coastal setting (Mont-Saint-Michel Bay, France). *Geology* 37,
 1010 1031–1034.
- 1011 Blaauw, M., 2010. Methods and code for ‘classical’ age-modelling of radiocarbon sequences.
 1012 *quaternary geochronology* 5, 512–518.
- 1013 Blaauw, M., Christen, J.A., 2011. Flexible paleoclimate age-depth models using an
 1014 autoregressive gamma process. *Bayesian analysis* 6, 457–474.
- 1015 Bond, G., 2001. Persistent Solar Influence on North Atlantic Climate During the Holocene.
 1016 *Science* 294, 2130–2136. <https://doi.org/10.1126/science.1065680>
- 1017 Bond, G., 1997. A Pervasive Millennial-Scale Cycle in North Atlantic Holocene and Glacial
 1018 Climates. *Science* 278, 1257–1266. <https://doi.org/10.1126/science.278.5341.1257>
- 1019 Bout-Roumazeilles, V., Combourieu-Nebout, N., Desprat, S., Siani, G., Turon, J.-L., Essallami,
 1020 L., 2013. Tracking atmospheric and riverine terrigenous supplies variability during the last
 1021 glacial and the Holocene in central Mediterranean.
- 1022 Brayshaw, D.J., Woollings, T., Vellinga, M., 2009. Tropical and Extratropical Responses of the
 1023 North Atlantic Atmospheric Circulation to a Sustained Weakening of the MOC. *Journal of*
 1024 *Climate* 22, 3146–3155. <https://doi.org/10.1175/2008JCLI2594.1>
- 1025 Brönnimann, S., Xoplaki, E., Casty, C., Pauling, A., Luterbacher, J., 2007. ENSO influence on
 1026 Europe during the last centuries. *Climate Dynamics* 28, 181–197.
- 1027 Bueh, C., Nakamura, H., 2007. Scandinavian pattern and its climatic impact. *Quarterly Journal*
 1028 *of the Royal Meteorological Society* 133, 2117–2131.
- 1029 Cassou, C., Terray, L., 2001. Dual influence of Atlantic and Pacific SST anomalies on the North
 1030 Atlantic/Europe winter climate. *Geophysical research letters* 28, 3195–3198.
- 1031 Cassou, C., Terray, L., Phillips, A.S., 2005. Tropical Atlantic influence on European heat
 1032 waves. *Journal of climate* 18, 2805–2811.
- 1033 Cazelles, B., Chavez, M., Berteaux, D., Ménard, F., Vik, J.O., Jenouvrier, S., Stenseth, N.C.,
 1034 2008. Wavelet analysis of ecological time series. *Oecologia* 156, 287–304.
- 1035 Chamley, H., 1971. Recherches sur la sédimentation argileuse en Méditerranée. *Persée-Portail*
 1036 *des revues scientifiques en SHS*.
- 1037 Combourieu Nebout, N., Peyron, O., Dormoy, I., Desprat, S., Beaudouin, C., Kotthoff, U.,
 1038 Marret, F., 2009. Rapid climatic variability in the west Mediterranean during the last 25
 1039 000 years from high resolution pollen data. *Climate of the Past* 5, 503–521.

- 1040 Conte, M., Giuffrida, A., Tedesco, S., 1989. Mediterranean Oscillation: Impact on Precipitation
1041 and Hydrology in Italy, in: Conference on Climate and Water.
- 1042 Conte, M.H., Sicre, M.-A., Rühlemann, C., Weber, J.C., Schulte, S., Schulz-Bull, D., Blanz, T.,
1043 2006. Global temperature calibration of the alkenone unsaturation index (UK' 37) in
1044 surface waters and comparison with surface sediments. *Geochemistry, Geophysics,*
1045 *Geosystems* 7.
- 1046 Costas, S., Naughton, F., Goble, R., Renssen, H., 2016. Windiness spells in SW Europe since
1047 the last glacial maximum. *Earth and Planetary Science Letters* 436, 82–92.
- 1048 Czymzik, M., Muscheler, R., Brauer, A., 2016. Solar modulation of flood frequency in central
1049 Europe during spring and summer on interannual to multi-centennial timescales. *Climate*
1050 *of the Past* 12, 799–805.
- 1051 Debret, M., Bout-Roumazeilles, V., Grousset, F., Desmet, M., McManus, J.F., Massei, N.,
1052 Sebag, D., Petit, J.-R., Copard, Y., Trentesaux, A., 2007. The origin of the 1500-year
1053 climate cycles in Holocene North-Atlantic records. *Climate of the Past Discussions* 3, 679–
1054 692.
- 1055 Debret, M., Sebag, D., Crosta, X., Massei, N., Petit, J.-R., Chapron, E., Bout-Roumazeilles, V.,
1056 2009. Evidence from wavelet analysis for a mid-Holocene transition in global climate
1057 forcing. *Quaternary Science Reviews* 28, 2675–2688.
1058 <https://doi.org/10.1016/j.quascirev.2009.06.005>
- 1059 Degeai, J.-P., Devillers, B., Dezileau, L., Oueslati, H., Bony, G., 2015. Major storm periods and
1060 climate forcing in the Western Mediterranean during the Late Holocene. *Quaternary*
1061 *Science Reviews* 129, 37–56. <https://doi.org/10.1016/j.quascirev.2015.10.009>
- 1062 deMenocal, P., Ortiz, J., Guilderson, T., Adkins, J., Sarnthein, M., Baker, L., Yarusinsky, M.,
1063 2000. Abrupt onset and termination of the African Humid Period:: rapid climate responses
1064 to gradual insolation forcing. *Quaternary science reviews* 19, 347–361.
- 1065 Deser, C., Capotondi, A., Saravanan, R., Phillips, A.S., 2006. Tropical Pacific and Atlantic
1066 climate variability in CCSM3. *Journal of Climate* 19, 2451–2481.
- 1067 Dezileau, L., Pérez-Ruzafa, A., Blanchemanche, P., Degeai, J.-P., Raji, O., Martinez, P.,
1068 Marcos, C., Von Grafenstein, U., 2016. Extreme storms during the last 6500 years from
1069 lagoonal sedimentary archives in the Mar Menor (SE Spain). *Climate of the Past* 12, 1389–
1070 1400. <https://doi.org/10.5194/cp-12-1389-2016>
- 1071 Dezileau, L., Sabatier, P., Blanchemanche, P., Joly, B., Swingedouw, D., Cassou, C., Castaings,
1072 J., Martinez, P., Von Grafenstein, U., 2011. Intense storm activity during the Little Ice Age
1073 on the French Mediterranean coast. *Palaeogeography, Palaeoclimatology, Palaeoecology*
1074 299, 289–297. <https://doi.org/10.1016/j.palaeo.2010.11.009>
- 1075 Farge, M., 1992. Wavelet transforms and their applications to turbulence. *Annual review of*
1076 *fluid mechanics* 24, 395–458.
- 1077 Fletcher, W.J., Debret, M., Goñi, M.F.S., 2013. Mid-Holocene emergence of a low-frequency
1078 millennial oscillation in western Mediterranean climate: Implications for past dynamics of
1079 the North Atlantic atmospheric westerlies. *The Holocene* 23, 153–166.
- 1080 Foster, G., 1996. Wavelets for period analysis of unevenly sampled time series. *The*
1081 *Astronomical Journal* 112, 1709.
- 1082 Fraedrich, K., 1994. An ENSO impact on Europe? *Tellus A* 46, 541–552.
- 1083 Fraedrich, K., 1990. European grosswetter during the warm and cold extremes of the El
1084 Niño/Southern Oscillation. *International Journal of Climatology* 10, 21–31.
- 1085 Fraedrich, K., Müller, K., 1992. Climate anomalies in Europe associated with ENSO extremes.
1086 *International Journal of Climatology* 12, 25–31.
- 1087 Franke, J.G., Werner, J.P., Donner, R.V., 2017. Reconstructing Late Holocene North Atlantic
1088 atmospheric circulation changes using functional paleoclimate networks. *Climate of the*
1089 *Past* 13, 1593–1608. <https://doi.org/10.5194/cp-13-1593-2017>

1090 Frigola, J., Moreno, A., Cacho, I., Canals, M., Sierro, F.J., Flores, J.A., Grimalt, J.O., Hodell,
1091 D.A., Curtis, J.H., 2007. Holocene climate variability in the western Mediterranean region
1092 from a deepwater sediment record: HOLOCENE CLIMATE VARIABILITY.
1093 *Paleoceanography* 22. <https://doi.org/10.1029/2006PA001307>

1094 Gagosian, R.B., Peltzer, E.T., 1986. The importance of atmospheric input of terrestrial organic
1095 material to deep sea sediments. *Organic Geochemistry* 10, 661–669.

1096 Ghaderpour, E., Ince, E.S., Pagiatakis, S.D., 2018. Least-squares cross-wavelet analysis and its
1097 applications in geophysical time series. *Journal of Geodesy* 92, 1223–1236.

1098 Ghaderpour, E., Pagiatakis, S.D., 2019. LSWAVE: a MATLAB software for the least-squares
1099 wavelet and cross-wavelet analyses. *GPS Solutions* 23, 50.

1100 Giraudi, C., 2005. Middle to Late Holocene glacial variations, periglacial processes and alluvial
1101 sedimentation on the higher Apennine massifs (Italy). *Quaternary Research* 64, 176–184.

1102 Giraudi, C., Magny, M., Zanchetta, G., Drysdale, R.N., 2011. The Holocene climatic evolution
1103 of Mediterranean Italy: A review of the continental geological data. *The Holocene* 21,
1104 105–115.

1105 Gouirand, I., Moron, V., 2003. Variability of the impact of El Niño–southern oscillation on sea-
1106 level pressure anomalies over the North Atlantic in January to March (1874–1996).
1107 *International journal of climatology* 23, 1549–1566.

1108 GROUP, M., 1970. Observation of formation of deep water in the Mediterranean Sea, 1969.

1109 Harvey, B.J., Shaffrey, L.C., Woollings, T.J., 2015. Deconstructing the climate change response
1110 of the Northern Hemisphere wintertime storm tracks. *Climate dynamics* 45, 2847–2860.

1111 Hasselmann, K., 1976. Stochastic climate models part I. Theory. *tellus* 28, 473–485.

1112 Held, I.M., Ting, M., Wang, H., 2002. Northern winter stationary waves: Theory and modeling.
1113 *Journal of climate* 15, 2125–2144.

1114 Hochman, A., Saaroni, H., Abramovich, F., Alpert, P., 2019. Artificial Detection of Lower-
1115 Frequency Periodicity in Climatic Studies by Wavelet Analysis Demonstrated on Synthetic
1116 Time Series. *Journal of Applied Meteorology and Climatology* 58, 2077–2086.

1117 Honda, M., Nakamura, H., Ukita, J., Kousaka, I., Takeuchi, K., 2001. Interannual seesaw
1118 between the Aleutian and Icelandic lows. Part I: Seasonal dependence and life cycle.
1119 *Journal of climate* 14, 1029–1042.

1120 Hurrell, J.W., Kushnir, Y., Ottersen, G., Visbeck, M., 2003. An overview of the North Atlantic
1121 oscillation. *The North Atlantic Oscillation: climatic significance and environmental impact*
1122 134, 1–35.

1123 Jalali, B., Sicre, M.-A., Bassetti, M.-A., Kallel, N., 2016. Holocene climate variability in the
1124 north-western Mediterranean Sea (gulf of lions). *Climate of the Past Discussions* 91–120.

1125 Jalali, B., Sicre, M.-A., Kallel, N., Azuara, J., Combourieu-Nebout, N., Bassetti, M.-A., Klein,
1126 V., 2017. High-resolution Holocene climate and hydrological variability from two major
1127 Mediterranean deltas (Nile and Rhone). *The Holocene* 0959683616683258.

1128 Jalut, G., Dedoubat, J.J., Fontugne, M., Otto, T., 2009. Holocene circum-Mediterranean
1129 vegetation changes: Climate forcing and human impact. *Quaternary International* 200, 4–
1130 18. <https://doi.org/10.1016/j.quaint.2008.03.012>

1131 Jaouadi, S., Lebreton, V., Bout-Roumzeilles, V., Siani, G., Lakhdar, R., Boussoffara, R.,
1132 Dezileau, L., Kallel, N., Mannai-Tayech, B., Combourieu-Nebout, N., 2016.
1133 Environmental changes, climate and anthropogenic impact in south-east Tunisia during the
1134 last 8 kyr. *Climate of the Past* 12, 1339–1359. <https://doi.org/10.5194/cp-12-1339-2016>

1135 Jiménez-Moreno, G., Rodríguez-Ramírez, A., Pérez-Asensio, J.N., Carrión, J.S., López-Sáez,
1136 J.A., Villarías-Robles, J.J., Celestino-Pérez, S., Cerrillo-Cuenca, E., León, Á., Contreras,
1137 C., 2015. Impact of late-Holocene aridification trend, climate variability and geodynamic
1138 control on the environment from a coastal area in SW Spain. *The Holocene* 25, 607–617.

- 1139 Joly, B., Girardot, N., Roulet, B., Labadie, C., 2012. Experimental Daily Forecasts of Northern
 1140 Atlantic Weather Regimes and Heavy Precipitating Events (HPEs) over Southern France
 1141 with the Meteo France Global Ensemble System PEARP.
- 1142 Kelly, B.C., Bechtold, J., Siemiginowska, A., 2009. Are the variations in quasar optical flux
 1143 driven by thermal fluctuations? *The Astrophysical Journal* 698, 895.
- 1144 Kelly, B.C., Becker, A.C., Sobolewska, M., Siemiginowska, A., Uttley, P., 2014. Flexible and
 1145 scalable methods for quantifying stochastic variability in the era of massive time-domain
 1146 astronomical data. *ApJ* 788, 33. <https://doi.org/10.1088/0004-637X/788/1/33>
- 1147 Lebeaupin Brossier, C., Drobinski, P., 2009. Numerical high-resolution air-sea coupling over
 1148 the Gulf of Lions during two tramontane/mistral events. *Journal of Geophysical Research:*
 1149 *Atmospheres* 114.
- 1150 Lenoir, G., Crucifix, M., 2018a. A general theory on frequency and time–frequency analysis of
 1151 irregularly sampled time series based on projection methods–Part 1: Frequency analysis.
 1152 *Nonlinear Processes in Geophysics* 25, 145.
- 1153 Lenoir, G., Crucifix, M., 2018b. A general theory on frequency and time–frequency analysis of
 1154 irregularly sampled time series based on projection methods–Part 2: Extension to time–
 1155 frequency analysis. *Nonlinear Processes in Geophysics* 25.
- 1156 Lionello, P., Trigo, I.F., Gil, V., Liberato, M.L.R., Nissen, K.M., Pinto, J.G., Raible, C.C.,
 1157 Reale, M., Tanzarella, A., Trigo, R.M., Ulbrich, S., Ulbrich, U., 2016. Objective
 1158 climatology of cyclones in the Mediterranean region: a consensus view among methods
 1159 with different system identification and tracking criteria. *Tellus A: Dynamic Meteorology*
 1160 *and Oceanography* 68, 29391. <https://doi.org/10.3402/tellusa.v68.29391>
- 1161 Lomb, N.R., 1976. Least-squares frequency analysis of unequally spaced data. *Astrophysics and*
 1162 *space science* 39, 447–462.
- 1163 Loon, H., Madden, R.A., 1981. The Southern Oscillation. Part I: Global associations with
 1164 pressure and temperature in northern winter. *Monthly Weather Review* 109, 1150–1162.
- 1165 Ludwig, W., Dumont, E., Meybeck, M., Heussner, S., 2009. River discharges of water and
 1166 nutrients to the Mediterranean and Black Sea: major drivers for ecosystem changes during
 1167 past and future decades? *Progress in Oceanography* 80, 199–217.
- 1168 Magny, M., Bégeot, C., Guiot, J., Peyron, O., 2003. Contrasting patterns of hydrological
 1169 changes in Europe in response to Holocene climate cooling phases. *Quaternary Science*
 1170 *Reviews* 22, 1589–1596. [https://doi.org/10.1016/S0277-3791\(03\)00131-8](https://doi.org/10.1016/S0277-3791(03)00131-8)
- 1171 Magny, M., Combourieu-Nebout, N., De Beaulieu, J.L., Bout-Roumazeilles, V., Colombaroli,
 1172 D., Desprat, S., Francke, A., Joannin, S., Peyron, O., Revel, M., 2013. North-south
 1173 palaeohydrological contrasts in the central Mediterranean during the Holocene: tentative
 1174 synthesis and working hypotheses. *Climate of the Past Discussions* 9, 1901–1967.
- 1175 Magny, M., de Beaulieu, J.-L., Drescher-Schneider, R., Vanni ere, B., Walter-Simonnet, A.-V.,
 1176 Miras, Y., Millet, L., Bossuet, G., Peyron, O., Brugiapaglia, E., Leroux, A., 2007.
 1177 Holocene climate changes in the central Mediterranean as recorded by lake-level
 1178 fluctuations at Lake Accessa (Tuscany, Italy). *Quaternary Science Reviews* 26, 1736–1758.
 1179 <https://doi.org/10.1016/j.quascirev.2007.04.014>
- 1180 Magny, M., Miramont, C., Sivan, O., 2002. Assessment of the impact of climate and
 1181 anthropogenic factors on Holocene Mediterranean vegetation in Europe on the basis of
 1182 palaeohydrological records. *Palaeogeography, Palaeoclimatology, Palaeoecology* 186, 47–
 1183 59.
- 1184 Magny, M., Peyron, O., Sadori, L., Ortu, E., Zanchetta, G., Vanni ere, B., Tinner, W., 2012.
 1185 Contrasting patterns of precipitation seasonality during the Holocene in the south- and
 1186 north-central Mediterranean. *Journal of Quaternary Science* 27, 290–296.
 1187 <https://doi.org/10.1002/jqs.1543>

1188 Mann, M.E., Bradley, R.S., Hughes, M.K., 2000. Long-term variability in the El Niño Southern
1189 Oscillation and associated teleconnections. Cambridge University Press, Cambridge, UK.

1190 Manzini, E., Giorgetta, M.A., Esch, M., Kornbluh, L., Roeckner, E., 2006. The influence of
1191 sea surface temperatures on the northern winter stratosphere: Ensemble simulations with
1192 the MAECHAM5 model. *Journal of climate* 19, 3863–3881.

1193 Maraun, D., Kurths, J., 2004. Cross wavelet analysis: significance testing and pitfalls.

1194 Mariotti, A., Ballabrera-Poy, J., Zeng, N., 2005. Tropical influence on Euro-Asian autumn
1195 rainfall variability. *Climate Dynamics* 24, 511–521.

1196 Mariotti, A., Zeng, N., Lau, K.-M., 2002. Euro-Mediterranean rainfall and ENSO—a seasonally
1197 varying relationship. *Geophysical research letters* 29.

1198 Martin-Puertas, C., Matthes, K., Brauer, A., Muscheler, R., Hansen, F., Petrick, C., Aldahan, A.,
1199 Possnert, G., van Geel, B., 2012. Regional atmospheric circulation shifts induced by a
1200 grand solar minimum. *Nature Geoscience* 5, 397–401. <https://doi.org/10.1038/ngeo1460>

1201 Martin-Vide, J., Lopez-Bustins, J.-A., 2006. The western Mediterranean oscillation and rainfall
1202 in the Iberian Peninsula. *International Journal of Climatology* 26, 1455–1475.

1203 Mary, Y., Eynaud, F., Colin, C., Rossignol, L., Brocheray, S., Mojtahid, M., Garcia, J., Peral,
1204 M., Howa, H., Zaragosi, S., Cremer, M., 2017. Changes in Holocene meridional circulation
1205 and poleward Atlantic flow: the Bay of Biscay as a nodal point. *Climate of the Past* 13,
1206 201–216. <https://doi.org/10.5194/cp-13-201-2017>

1207 Mathias, A., Grond, F., Guardans, R., Seese, D., Canela, M., Diebner, H.H., Baiocchi, G., 2004.
1208 Algorithms for spectral analysis of irregularly sampled time series. *Journal of Statistical*
1209 *Software* 11, 1–30.

1210 May, W., Bengtsson, L., 1998. The signature of ENSO in the Northern Hemisphere midlatitude
1211 seasonal mean flow and high-frequency intraseasonal variability. *Meteorology and*
1212 *Atmospheric Physics* 69, 81–100.

1213 Mayewski, P.A., Rohling, E.E., Curt Stager, J., Karlén, W., Maasch, K.A., Meeker, L.D.,
1214 Meyerson, E.A., Gasse, F., van Kreveld, S., Holmgren, K., Lee-Thorp, J., Rosqvist, G.,
1215 Rack, F., Staubwasser, M., Schneider, R.R., Steig, E.J., 2004. Holocene Climate
1216 Variability. *Quaternary Research* 62, 243–255. <https://doi.org/10.1016/j.yqres.2004.07.001>

1217 Moron, V., Gouirand, I., 2003. Seasonal modulation of the El Niño–Southern Oscillation
1218 relationship with sea level pressure anomalies over the North Atlantic in October–March
1219 1873–1996. *International Journal of Climatology* 23, 143–155.

1220 Moy, C.M., Seltzer, G.O., Rodbell, D.T., Anderson, D.M., 2002. Variability of El
1221 Niño/Southern Oscillation activity at millennial timescales during the Holocene epoch.
1222 *Nature* 420, 162–165.

1223 Mudelsee, M., Scholz, D., Röthlisberger, R., Fleitmann, D., Mangini, A., Wolff, E.W., 2009.
1224 Climate spectrum estimation in the presence of timescale errors. *Nonlinear Processes in*
1225 *Geophysics* 16, 43–56.

1226 Muñoz-Díaz, D., Rodrigo, F.S., 2005. Influence of the El Niño–Southern Oscillation on the
1227 probability of dry and wet seasons in Spain. *Climate Research* 30, 1–12.

1228 Najac, J., Boé, J., Terray, L., 2009. A multi-model ensemble approach for assessment of climate
1229 change impact on surface winds in France. *Climate Dynamics* 32, 615–634.
1230 <https://doi.org/10.1007/s00382-008-0440-4>

1231 Nigam, S., DeWeaver, E., 2003. Stationary waves (orographic and thermally forced).

1232 Nissen, K.M., Leckebusch, G.C., Pinto, J.G., Renggli, D., Ulbrich, S., Ulbrich, U., 2010.
1233 Cyclones causing wind storms in the Mediterranean: characteristics, trends and links to
1234 large-scale patterns. *Natural Hazards and Earth System Science* 10, 1379–1391.

1235 Nuissier, O., Joly, B., Joly, A., Ducrocq, V., Arbogast, P., 2011. A statistical downscaling to
1236 identify the large-scale circulation patterns associated with heavy precipitation events over

- 1237 southern France. *Quarterly Journal of the Royal Meteorological Society* 137, 1812–1827.
 1238 <https://doi.org/10.1002/qj.866>
- 1239 Ólafsdóttir, K.B., Schulz, M., Mudelsee, M., 2016. REDFIT-X: Cross-spectral analysis of
 1240 unevenly spaced paleoclimate time series. *Computers & Geosciences* 91, 11–18.
- 1241 Oppenheim, A.V., 1999. *Discrete-time signal processing*. Pearson Education India.
- 1242 Orme, L.C., Reinhardt, L., Jones, R.T., Charman, D.J., Barkwith, A., Ellis, M.A., 2016. Aeolian
 1243 sediment reconstructions from the Scottish Outer Hebrides: Late Holocene storminess and
 1244 the role of the North Atlantic Oscillation. *Quaternary Science Reviews* 132, 15–25.
- 1245 Ortega, P., Lehner, F., Swingedouw, D., Masson-Delmotte, V., Raible, C.C., Casado, M., Yiou,
 1246 P., 2015. A model-tested North Atlantic Oscillation reconstruction for the past millennium.
 1247 *Nature* 523, 71–74.
- 1248 Pardo-Igúzquiza, E., Rodríguez-Tovar, F.J., 2012. Spectral and cross-spectral analysis of
 1249 uneven time series with the smoothed Lomb–Scargle periodogram and Monte Carlo
 1250 evaluation of statistical significance. *Computers & geosciences* 49, 207–216.
- 1251 Peyron, O., Magny, M., Goring, S., Joannin, S., de Beaulieu, J.-L., Brugiapaglia, E., Sadori, L.,
 1252 Garfi, G., Kouli, K., Ioakim, C., Combourieu-Nebout, N., 2013. Contrasting patterns of
 1253 climatic changes during the Holocene across the Italian Peninsula reconstructed from
 1254 pollen data. *Climate of the Past* 9, 1233–1252. <https://doi.org/10.5194/cp-9-1233-2013>
- 1255 Plaut, G., Simonnet, E., 2001. Large-scale circulation classification, weather regimes, and local
 1256 climate over France, the Alps and Western Europe. *Climate Research* 17, 303–324.
- 1257 Polanco-Martínez, J.M., Faria, S.H., 2018. Estimation of the significance of the Foster’s
 1258 wavelet spectrum by means of the permutation test, and applications to paleoclimate
 1259 records.
- 1260 Pozo-Vázquez, D., Gámiz-Fortis, S.R., Tovar-Pescador, J., Esteban-Parra, M.J., Castro-Díez,
 1261 Y., 2005. El Niño–Southern Oscillation events and associated European winter
 1262 precipitation anomalies. *International Journal of Climatology* 25, 17–31.
- 1263 Raible, C.C., Luksch, U., Fraedrich, K., 2004. Precipitation and northern hemisphere regimes.
 1264 *Atmospheric Science Letters* 5, 43–55.
- 1265 Raible, C.C., Luksch, U., Fraedrich, K., Voss, R., 2001. North Atlantic decadal regimes in a
 1266 coupled GCM simulation. *Climate Dynamics* 18, 321–330.
- 1267 Raible, C.C., Yoshimori, M., Stocker, T.F., Casty, C., 2007. Extreme midlatitude cyclones and
 1268 their implications for precipitation and wind speed extremes in simulations of the Maunder
 1269 Minimum versus present day conditions. *Climate Dynamics* 28, 409–423.
 1270 <https://doi.org/10.1007/s00382-006-0188-7>
- 1271 Raji, O., Dezileau, L., Von Grafenstein, U., Niazi, S., Snoussi, M., Martinez, P., 2015. Extreme
 1272 sea events during the last millennium in the northeast of Morocco. *Natural Hazards and*
 1273 *Earth System Sciences* 15, 203.
- 1274 Rameau, J.-C., Mansion, D., Dumé, G., 1989. *Flore forestière française: région*
 1275 *méditerranéenne. Forêt privée française*.
- 1276 Randel, W.J., Wu, F., Oltmans, S.J., Rosenlof, K., Nedoluha, G.E., 2004. Interannual changes
 1277 of stratospheric water vapor and correlations with tropical tropopause temperatures.
 1278 *Journal of the Atmospheric Sciences* 61, 2133–2148.
- 1279 Raynal, O., Bouchette, F., Certain, R., Séranne, M., Dezileau, L., Sabatier, P., Lofi, J., Hy,
 1280 A.B.X., Briquieu, L., Pezard, P., Tessier, B., 2009. Control of alongshore-oriented sand
 1281 spits on the dynamics of a wave-dominated coastal system (Holocene deposits, northern
 1282 Gulf of Lions, France). *Marine Geology* 264, 242–257.
 1283 <https://doi.org/10.1016/j.margeo.2009.06.008>
- 1284 Reimer, P.J., Bard, E., Bayliss, A., Beck, J.W., Blackwell, P.G., Ramsey, C.B., Buck, C.E.,
 1285 Cheng, H., Edwards, R.L., Friedrich, M., 2013. IntCal13 and Marine13 radiocarbon age
 1286 calibration curves 0–50,000 years cal BP. *Radiocarbon* 55, 1869–1887.

- 1287 Rhein, M., 1995. Deep water formation in the western Mediterranean. *Journal of Geophysical*
1288 *Research: Oceans* 100, 6943–6959.
- 1289 Rhines, A., Huybers, P., 2011. Estimation of spectral power laws in time uncertain series of data
1290 with application to the Greenland Ice Sheet Project 2 $\delta^{18}\text{O}$ record. *Journal of Geophysical*
1291 *Research: Atmospheres* 116.
- 1292 Rimbu, N., Lohmann, G., Felis, T., Pätzold, J., 2003. Shift in ENSO teleconnections recorded
1293 by a northern Red Sea coral. *Journal of Climate* 16, 1414–1422.
- 1294 Roberts, N., Brayshaw, D., Kuzucuoğlu, C., Perez, R., Sadori, L., 2011. The mid-Holocene
1295 climatic transition in the Mediterranean: Causes and consequences. *The Holocene* 21, 3–
1296 13. <https://doi.org/10.1177/0959683610388058>
- 1297 Roberts, N., Moreno, A., Valero-Garcés, B.L., Corella, J.P., Jones, M., Allcock, S.,
1298 Woodbridge, J., Morellón, M., Luterbacher, J., Xoplaki, E., 2012. Palaeolimnological
1299 evidence for an east–west climate see-saw in the Mediterranean since AD 900. *Global and*
1300 *Planetary Change* 84, 23–34.
- 1301 Rogers, J.C., 1997. North Atlantic storm track variability and its association to the North
1302 Atlantic Oscillation and climate variability of northern Europe. *Journal of Climate* 10,
1303 1635–1647.
- 1304 Sabatier, P., Bruno, W., Francesco, F.G., Fanny, M., Jérôme, P., Anne-Lise, D., Adeline, B.,
1305 Wentao, C., Cécile, P., Jean-Louis, R., Ludovic, G., Manon, B., Yves, P., Emmanuel, M.,
1306 Pierre, T., Fabien, A., 2017. 6-kyr record of flood frequency and intensity in the western
1307 Mediterranean Alps – Interplay of solar and temperature forcing. *Quaternary Science*
1308 *Reviews* 170, 121–135. <https://doi.org/10.1016/j.quascirev.2017.06.019>
- 1309 Sabatier, P., Dezileau, L., 2010. Archives sédimentaires dans les lagunes du Golfe d’Aigues-
1310 Mortes. Estimation de l’aléa de tempête depuis 2000 ans. *Quaternaire. Revue de*
1311 *l’Association française pour l’étude du Quaternaire* 21, 5–11.
- 1312 Sabatier, P., Dezileau, L., Briquieu, L., Colin, C., Siani, G., 2010. Clay minerals and
1313 geochemistry record from northwest Mediterranean coastal lagoon sequence: Implications
1314 for paleostorm reconstruction. *Sedimentary Geology* 228, 205–217.
1315 <https://doi.org/10.1016/j.sedgeo.2010.04.012>
- 1316 Sabatier, P., Dezileau, L., Colin, C., Briquieu, L., Bouchette, F., Martinez, P., Siani, G., Raynal,
1317 O., Von Grafenstein, U., 2012. 7000 years of paleostorm activity in the NW Mediterranean
1318 Sea in response to Holocene climate events. *Quaternary Research* 77, 1–11.
1319 <https://doi.org/10.1016/j.yqres.2011.09.002>
- 1320 Sabatier, P., Dezileau, L., Condomines, M., Briquieu, L., Colin, C., Bouchette, F., Le Duff, M.,
1321 Blanchemanche, P., 2008. Reconstruction of paleostorm events in a coastal lagoon
1322 (Hérault, South of France). *Marine Geology* 251, 224–232.
1323 <https://doi.org/10.1016/j.margeo.2008.03.001>
- 1324 Sabatier, P., Nicolle, M., Piot, C., Christophe, C., Debret, M., Swingedouw, D., Perrette, Y.,
1325 Bellingery, M.-C., Chazeau, B., Develle, A.-L., 2020. Past African dust inputs in the
1326 western Mediterranean area controlled by the complex interaction between the Intertropical
1327 Convergence Zone, the North Atlantic Oscillation, and total solar irradiance. *Climate of*
1328 *the Past* 16, 283–298.
- 1329 Sadori, L., Giardini, M., Gliozzi, E., Mazzini, I., Sulpizio, R., van Welden, A., Zanchetta, G.,
1330 2015. Vegetation, climate and environmental history of the last 4500 years at lake Shkodra
1331 (Albania/Montenegro). *The Holocene* 25, 435–444.
- 1332 Scargle, J.D., 1982. Studies in astronomical time series analysis. II-Statistical aspects of spectral
1333 analysis of unevenly spaced data. *The Astrophysical Journal* 263, 835–853.
- 1334 Schroeder, K., Josey, S.A., Herrmann, M., Grignon, L., Gasparini, G.P., Bryden, H.L., 2010.
1335 Abrupt warming and salting of the Western Mediterranean Deep Water after 2005:
1336 atmospheric forcings and lateral advection. *Journal of Geophysical Research: Oceans* 115.

1337 Schulz, M., Mudelsee, M., 2002. REDFIT: estimating red-noise spectra directly from unevenly
1338 spaced paleoclimatic time series. *Computers & Geosciences* 28, 421–426.

1339 Schulz, M., Stattgeger, K., 1997. SPECTRUM: Spectral analysis of unevenly spaced
1340 paleoclimatic time series. *Computers & Geosciences* 23, 929–945.

1341 Sgubin, G., Swingedouw, D., Drijfhout, S., Mary, Y., Bennabi, A., 2017. Abrupt cooling over
1342 the North Atlantic in modern climate models. *Nature Communications* 8.

1343 Siani, G., Magny, M., Paterne, M., Debret, M., Fontugne, M., 2013. Paleohydrology
1344 reconstruction and Holocene climate variability in the South Adriatic Sea. *Climate of the*
1345 *Past* 9, 499–515. <https://doi.org/10.5194/cp-9-499-2013>

1346 Sicre, M.-A., Jalali, B., Martrat, B., Schmidt, S., Bassetti, M.-A., Kallel, N., 2016. Sea surface
1347 temperature variability in the North Western Mediterranean Sea (Gulf of Lion) during the
1348 Common Era. *Earth and Planetary Science Letters* 456, 124–133.
1349 <https://doi.org/10.1016/j.epsl.2016.09.032>

1350 Smith, A.C., Wynn, P.M., Barker, P.A., Leng, M.J., Noble, S.R., Tych, W., 2016. North
1351 Atlantic forcing of moisture delivery to Europe throughout the Holocene. *Scientific*
1352 *Reports* 6. <https://doi.org/10.1038/srep24745>

1353 Solanki, S.K., Usoskin, I.G., Kromer, B., Schüssler, M., Beer, J., 2004. Unusual activity of the
1354 Sun during recent decades compared to the previous 11,000 years. *Nature* 431, 1084–1087.

1355 Sorrel, P., Debret, M., Billeaud, I., Jaccard, S.L., McManus, J.F., Tessier, B., 2012. Persistent
1356 non-solar forcing of Holocene storm dynamics in coastal sedimentary archives. *Nature*
1357 *Geoscience* 5, 892–896. <https://doi.org/10.1038/ngeo1619>

1358 Sorrel, P., Tessier, B., Demory, F., Delsinne, N., Mouazé, D., 2009. Evidence for millennial-
1359 scale climatic events in the sedimentary infilling of a macrotidal estuarine system, the
1360 Seine estuary (NW France). *Quaternary Science Reviews* 28, 499–516.

1361 Steinhilber, F., Abreu, J.A., Beer, J., Brunner, I., Christl, M., Fischer, H., Heikkilä, U., Kubik,
1362 P.W., Mann, M., McCracken, K.G., 2012. 9,400 years of cosmic radiation and solar
1363 activity from ice cores and tree rings. *Proceedings of the National Academy of Sciences*
1364 109, 5967–5971.

1365 Stocker, T.F., Qin, D., Plattner, G.K., Tignor, M., Allen, S.K., Boschung, J., Nauels, A., Xia,
1366 Y., Bex, V., Midgley, P.M., 2013. IPCC, 2013: summary for policymakers in climate
1367 change 2013: the physical science basis, contribution of working group I to the fifth
1368 assessment report of the intergovernmental panel on climate change. Cambridge University
1369 Press, Cambridge, New York, USA.

1370 Stuiver, M., Braziunas, T.F., 1989. Atmospheric ¹⁴C and century-scale solar oscillations.
1371 *Nature* 338, 405–408.

1372 Toreti, A., Xoplaki, E., Maraun, D., Kuglitsch, F.-G., Wanner, H., Luterbacher, J., 2010.
1373 Characterisation of extreme winter precipitation in Mediterranean coastal sites and
1374 associated anomalous atmospheric circulation patterns. *Natural Hazards and Earth System*
1375 *Sciences* 10, 1037–1050.

1376 Torrence, C., Compo, G.P., 1998. A practical guide to wavelet analysis. *Bulletin of the*
1377 *American Meteorological society* 79, 61–78.

1378 Torrence, C., Webster, P.J., 1999. Interdecadal changes in the ENSO–monsoon system. *Journal*
1379 *of climate* 12, 2679–2690.

1380 Trigo, I.F., Davies, T.D., Bigg, G.R., 1999. Objective climatology of cyclones in the
1381 Mediterranean region. *Journal of Climate* 12, 1685–1696.

1382 Trigo, R.M., DaCamara, C., 2000. Circulation weather types and their influence on the
1383 precipitation regime in Portugal. *International Journal of Climatology* 20, 1559–1581.

1384 Tsonis, A.A., 2009. Dynamical changes in the ENSO system in the last 11,000 years. *Climate*
1385 *dynamics* 33, 1069.

1386 Ulses, C., Estournel, C., Puig, P., Durrieu de Madron, X., Marsaleix, P., 2008. Dense shelf
1387 water cascading in the northwestern Mediterranean during the cold winter 2005:
1388 Quantification of the export through the Gulf of Lion and the Catalan margin. *Geophysical*
1389 *Research Letters* 35.

1390 Usoskin, I.G., Gallet, Y., Lopes, F., Kovaltsov, G.A., Hulot, G., 2016. Solar activity during the
1391 Holocene: the Hallstatt cycle and its consequence for grand minima and maxima.
1392 *Astronomy & Astrophysics* 587, A150.

1393 Vanniere, B., Galop, D., Rendu, C., Davasse, B., 2001. Feu et pratiques agro-pastorales dans les
1394 Pyrénées-Orientales: le cas de la montagne d'Enveitg (Cerdagne, Pyrénées-Orientales,
1395 France). *Sud-Ouest Européen* 11, 29–42.

1396 Walker, M.J., Berkelhammer, M., Björck, S., Cwynar, L.C., Fisher, D.A., Long, A.J., Lowe,
1397 J.J., Newnham, R.M., Rasmussen, S.O., Weiss, H., 2012. Formal subdivision of the
1398 Holocene Series/Epoch: a Discussion Paper by a Working Group of INTIMATE
1399 (Integration of ice-core, marine and terrestrial records) and the Subcommittee on
1400 Quaternary Stratigraphy (International Commission on Stratigraphy). *Journal of*
1401 *Quaternary Science* 27, 649–659.

1402 Welch, P., 1967. The use of fast Fourier transform for the estimation of power spectra: a method
1403 based on time averaging over short, modified periodograms. *IEEE Transactions on audio*
1404 *and electroacoustics* 15, 70–73.

1405 Winschall, A., Sodemann, H., Pfahl, S., Wernli, H., 2014. How important is intensified
1406 evaporation for Mediterranean precipitation extremes? *Journal of Geophysical Research:*
1407 *Atmospheres* 119, 5240–5256. <https://doi.org/10.1002/2013JD021175>

1408 Wirth, S.B., Glur, L., Gilli, A., Anselmetti, F.S., 2013. Holocene flood frequency across the
1409 Central Alps–solar forcing and evidence for variations in North Atlantic atmospheric
1410 circulation. *Quaternary Science Reviews* 80, 112–128.

1411 Witt, A., Schumann, A.Y., 2005. Holocene climate variability on millennial scales recorded in
1412 Greenland ice cores.

1413 Woollings, T., Gregory, J.M., Pinto, J.G., Reyers, M., Brayshaw, D.J., 2012. Response of the
1414 North Atlantic storm track to climate change shaped by ocean–atmosphere coupling.
1415 *Nature Geoscience* 5, 313–317. <https://doi.org/10.1038/ngeo1438>

1416 Xoplaki, E., 2002. Climate variability over the Mediterranean. PhD, University of Bern,
1417 Switzerland.

1418 Zazo, C., Dabrio, C.J., Goy, J.L., Lario, J., Cabero, A., Silva, P.G., Bardají, T., Mercier, N.,
1419 Borja, F., Roquero, E., 2008. The coastal archives of the last 15 ka in the Atlantic–
1420 Mediterranean Spanish linkage area: Sea level and climate changes. *Quaternary*
1421 *International* 181, 72–87.

1422 Zhang, Z., Moore, J., 2011. Intrinsic feature extraction in the COI of wavelet power spectra of
1423 climatic signals, in: 2011 4th International Congress on Image and Signal Processing.
1424 *IEEE*, pp. 2354–2356.

1425 Zielhofer, C., Fletcher, W.J., Mischke, S., De Batist, M., Campbell, J.F., Joannin, S., Tjallingii,
1426 R., El Hamouti, N., Junginger, A., Stele, A., 2017. Atlantic forcing of Western
1427 Mediterranean winter rain minima during the last 12,000 years. *Quaternary Science*
1428 *Reviews* 157, 29–51.

1429